Materials Advances

ROYAL SOCIETY OF CHEMISTRY

REVIEW

View Article Online
View Journal | View Issue

Cite this: *Mater. Adv.*, 2025, 6, 5807

Advancing ovarian cancer care: recent innovations and challenges in the use of MXenes and their composites for diagnostic and therapeutic applications

Neda Farzizadeh,[a] Atefeh Zarepour,[bc] Arezoo Khosravi,[de] Siavash Iravani *[f] and Ali Zarrabi *[g]

Ovarian cancer remains the deadliest form of gynecologic malignancy, largely owing to the absence of reliable early diagnostic tools and the limited effectiveness of current therapeutic strategies. Recent advances in nanotechnology—particularly the emergence of two-dimensional materials known as MXenes—offer promising avenues to address these challenges. This review highlights the emerging role of MXenes and their composites in the management of ovarian cancer, focusing on their potential in biomarker detection and targeted treatment strategies. We provide a comprehensive analysis of the latest studies examining the physicochemical features of MXenes, their synthesis and surface functionalization approaches, and their application in ovarian cancer, including biosensing, drug delivery, and combinatorial therapeutic systems. MXene-based biosensors have shown remarkable detection limits in detecting ovarian cancer biomarkers, such as cancer antigen 125 (CA125), human epididymis protein 4 (HE4), lipolysis-stimulated lipoprotein receptor (LSR), and carcinoembryonic antigen-related cell adhesion molecule 5 (CEACAM5). However, several challenges remain, including issues of biocompatibility, structural stability, and clinical scalability. Continued interdisciplinary research is essential to address these limitations, optimize MXene functionalization, and translate their laboratory success into clinical settings. With appropriate advancements, MXenes hold significant promise for enabling more precise, efficient, and patient-specific approaches to ovarian cancer diagnosis and therapy.

Received 21st May 2025,
Accepted 9th July 2025

DOI: 10.1039/d5ma00520e

rsc.li/materials-advances

1. Introduction

Among the three major gynecologic malignancies, ovarian cancer is the most lethal, despite being the third most commonly diagnosed.[1] According to the World Health Organization (WHO), over 324 000 new cases and more than 206 000 deaths were reported globally in 2022,[2] with mortality projected to exceed 313 000 by 2040.[3,4] The main causes of ovarian cancer's elevated mortality rate are its gradual progression, delayed onset of symptoms, and ineffective screening techniques, which frequently lead to an advanced stage diagnosis.[3] Owing to its position within the abdominal cavity, the initial manifestations of ovarian cancer are subtle, resulting in a diagnosis at an advanced stage in roughly 75% of patients that were characterized by extensive metastases, rendering simple surgical intervention insufficient for tumor eradication.[5] The WHO has categorized ovarian cancer into distinct types: epithelial tumors, mesenchymal tumors, mixed epithelial and mesenchymal tumors, sex-cord stromal tumors, germ cell tumors, monodermal teratoma and somatic-type tumors originating in dermoid cysts, various tumors, mesothelial neoplasms, tissue neoplasms, tumor-like lesions, lymphoid/myeloid neoplasms, and metastatic tumors.[6]

In patients exhibiting indicative symptoms, the diagnostic evaluation comprises a physical examination and radiographic imaging, including transvaginal ultrasonography (TVUS). A common screening strategy for the early detection of ovarian

[a] *Department of Midwifery, School of Nursing and Midwifery, Ardabil University of Medical Sciences, Ardabil, Iran*
[b] *Department of Biology, Faculty of Arts and Sciences, Kocaeli University, İzmit, Kocaeli, 41001, Türkiye*
[c] *Department of Research Analytics, Saveetha Dental College and Hospitals, Saveetha Institute of Medical and Technical Sciences, Saveetha University, Chennai 600 077, India*
[d] *Department of Genetics and Bioengineering, Faculty of Engineering and Natural Sciences, Istanbul Okan University, Istanbul 34959, Türkiye*
[e] *Graduate School of Biotechnology and Bioengineering, Yuan Ze University, Taoyuan 320315, Taiwan*
[f] *Independent Researcher, W Nazar ST, Boostan Ave, Isfahan, Iran. E-mail: siavashira@gmail.com*
[g] *Department of Biomedical Engineering, Faculty of Engineering and Natural Sciences, Istinye University, Istanbul 34396, Türkiye. E-mail: alizarrabi@gmail.com*

cancer is not yet available for asymptomatic women. At present, the Cancer Antigen 125 (CA125) blood test and TVUS are the most promising screening modalities for ovarian cancer detection.[7] More than 2 000 000 women globally undergo exploratory surgery for suspicious masses, resulting in nearly 300 000 new diagnoses of ovarian cancer; this highlights the critical need for improved non-invasive diagnostic tools to reduce unnecessary surgical interventions, mitigate patient risk, and alleviate healthcare burdens, particularly given that the majority of these procedures reveal benign conditions.[8,9] Ultrasound-based models can differentiate ovarian cancer from benign mimickers; however, preoperative diagnosis remains incomplete. Moreover, ovarian cancer manifests 5.1 years prior to the onset of clinical symptoms but may progress rapidly from early to late stages in less than a year. This creates a narrow but crucial window for early detection, which remains difficult to capture with current techniques.[9]

Despite these promising developments, ovarian cancer treatment still faces significant hurdles, including chemoresistance and metastasis, which are the leading causes of mortality. Current clinical strategies integrate debulking surgery, maximal cytoreductive surgery, platinum- and taxane-based chemotherapy, and targeted therapies like PARP inhibitors and antibody–drug conjugates, yet resistance often limits long-term success.[6] Debulking surgery removes as much of the tumor as possible, sometimes including the uterus and both ovaries, especially in advanced stages.[10] Maximal cytoreductive surgery removes all remaining disease, which greatly improves survival rates in patients in stages 3 and 4, and is frequently carried out after initial chemotherapy.[11] Chemotherapy mainly uses platinum-based agents like carboplatin or cisplatin in combination with taxanes like paclitaxel, which are administered intraperitoneally or intravenously to target cancer cells. Neoadjuvant chemotherapy, given before surgery, can also help shrink tumors and improve surgical outcomes.[12]

The current methods for diagnosis and treatment lack sufficient sensitivity and efficiency to detect ovarian cancer in its early stages. Furthermore, the elevated expenses and unspecified detection points resulted in delayed diagnosis.[13] Also, systemic therapies like chemotherapy and radiation therapy are associated with numerous adverse effects, including harm to healthy tissue, alopecia, nausea, and gastrointestinal complications. Researchers have increasingly turned to nanotechnology to develop more selective and efficient drug delivery systems.[14] By working at the nanoscale, it becomes possible to design materials with properties that significantly differ from their bulk counterparts, offering new opportunities for precise diagnosis and therapy.[15] Emerging technologies such as nanocarriers (nano-gels, aptamers, peptide-mediated formulations) and novel drug conjugates aim to enhance drug delivery specificity, reduce side effects, and improve pharmacokinetics by enabling sustained release near tumor sites. Clinical trials are actively investigating new agents targeting molecular subtypes of ovarian cancer, including CDK2 inhibitors and immunotherapy combinations, reflecting a shift towards personalized medicine. Parallel to these material innovations, advances in nanoparticle (NP)-packed hydrogels targeting female-specific biology offer new avenues for treating platinum-resistant ovarian cancer with fewer systemic toxicities, such as ocular side effects seen in current antibody–drug conjugates.[16]

Recent advancements in ovarian cancer care have focused on innovative targeted therapies and nanotechnology-based drug delivery systems to improve treatment efficacy and reduce side effects. Nanoparticles (NPs)—such as gold (Au), silver (Ag), carbon nanotubes, graphene oxide, quantum dots (QDs), and MXenes—have emerged as promising candidates in the fight against cancer due to their unique optical, electrical, and structural characteristics.[17–19] MXenes are a class of two-dimensional (2D) materials characterized by M representing an early transition metal, X denoting carbon or nitrogen, and -ene analogous to graphene, the first identified 2D substance.[14] MXenes possess an extensive surface area, high conductivity, outstanding photothermal conversion efficiency (PTCE), and strong near-infrared (NIR) absorption[15] that appropriate them for variety of biomedical applications, encompassing tumor identification as contrast agents, drug administration, biomedicine, cancer therapy, and diagnostics.[14,20–25] These 2D structures enable synergistic photothermal and chemotherapeutic approaches, targeted drug delivery, and enhanced bioimaging and biosensing capabilities. Researchers are exploring MXene-based systems for noninvasive, efficient cancer therapy, including photothermal therapy and controlled drug release. However, challenges remain regarding their stability in physiological environments, biodegradability, and the need for sustained and controlled drug delivery to maximize therapeutic outcomes.[26–29] Future perspectives emphasize overcoming biological barriers, improving MXene stability and biodegradability, and integrating multimodal therapies to enhance efficacy and patient quality of life.

The aim of this review is to explore recent advancements in the use of MXenes for the diagnosis and treatment of ovarian cancer. We highlight progress in synthesis and functionalization strategies aimed at improving their biocompatibility and therapeutic targeting, with a focus on the development of MXene-based biosensors and drug delivery platforms.

2. Overview of MXenes

2.1. Definition and structure of MXenes

MXenes are a family of 2D transition metal carbides, nitrides, or carbonitrides, first discovered by Naguib *et al.* in 2011 through the selective etching of MAX phases, layered ternary carbides or nitrides. The general formula for MAX phases is $M_{n+1}AX_n$ (n = 1, 2, or 3), where M is an early transition metal, A is a group 13 or 14 element (typically aluminum), and X is carbon and/or nitrogen. The resulting MXene, typically denoted as $M_{n+1}X_nT_x$, retains a layered structure after removal of the A layer, where T_x represents surface terminations such as –OH, –O, or –F introduced during synthesis.[30–32]

Structurally, MXenes feature strong M–X bonds (a mix of ionic and covalent interactions) and exhibit metallic conductivity due to their layered architecture.[33] The etching process commonly involves hydrofluoric acid (HF) or a combination of

fluoride salts and hydrochloric acid (HCl) to selectively remove the A layer from MAX phases (*e.g.*, Ti_3AlC_2), resulting in the formation of $Ti_3C_2T_x$, the most extensively studied MXene.[34]

To date, more than 50 MXene compositions have been experimentally synthesized by varying M and X elements, offering a broad platform for tailoring their chemical, electrical, and physical properties. Unlike other 2D materials such as graphene or transition metal dichalcogenides (TMDs), MAX phases exhibit strong interlayer bonding and cannot be exfoliated mechanically. Instead, MXenes are typically obtained *via* chemical exfoliation, producing nanosheets with a high degree of functional tunability.[30,35] All four of MXene's dimensions, 0D, 1D, 2D, and 3D, have been used in recent studies to examine its properties.[36] They exhibit several desirable properties for biomedical and technological applications, including hydrophilicity, paramagnetism, a large surface area, and a high atomic number due to the transition metal content. They also show exceptional electrical conductivity, corrosion resistance, and mechanical strength. The 2D morphology of MXenes offers a superior surface-to-volume ratio, enabling efficient interaction with biomolecules, critical for sensing, drug delivery, and biosensor platforms.[13,37,38] Therefore, the unique structural features and customizable surface chemistry of MXenes distinguish them from conventional 2D materials, making them highly attractive for diverse applications, including those in the biomedical field.

2.2. Synthesis and functionalization of MXenes

Two main strategies have been established for the synthesis of MXene compounds: top-down method and bottom-up method.[39] Each of these techniques has shown success in producing single-layer, few-layer, and multilayer MXene structures, so offering different advantages for fine-tuning material properties to fit intended uses.[35,40]

2.2.1. Top-down synthesis. Top-down synthesis is the most favored technique in which bulk materials are broken down into smaller structures, often by removing specific components from precursor materials. The primary goal is to selectively etch the A layer in the MAX phase precursor to produce MXenes.[41] Top-down synthesis uses several methods including HF etching, HF forming etchants, salt etchants, alkaline treatment, and electrochemical etching.[42]

Among these, HF etching is the most widely used due to its ability to effectively remove the A element and yield thin MXene flakes with functional surface groups such as hydrogen oxide, fluorine, and oxygen.[43] These intrinsic groups act as anchoring sites for additional functionalization, like covalent grafting, through diazonium salt reactions introduces organic groups (such as amines) to improve dispersibility,[44] or polymer wrapping, with poly(ethylene glycol) (PEG) that improves biocompatibility.[45,46] However, the use of HF raises safety concerns because of its corrosive and toxic nature, and the associated organic delaminating agents may introduce additional biocompatibility risks.[47] Although the human body contains trace fluoride ions, exposure to elevated levels from these procedures has been linked to oxidative stress, cellular damage, and organ toxicity.[48–50]

Ying *et al.* studied the removal of hexavalent chromium [Cr(VI)] using Ti_3C_2 nanosheets produced *via* HF etching and ultrasonic delamination. Their findings showed that the delaminated MXene could adsorb and reduce Cr(VI), achieving a final concentration well below WHO standards.[51] Mashtalir *et al.* examined exfoliation kinetics of Ti_3AlC_2 and found temperature, time, and particle size significantly influenced sheet formation and resistivity profiles. Electron microscopy confirmed structural exfoliation, while elemental analysis showed the presence of titanium, carbon, oxygen, and fluorine in the resulting materials.[52]

To improve safety and flake quality, researchers have turned to *in situ* HF generation by combining fluoride salts like lithium fluoride (LiF) with HCl, reducing the handling of HF directly.[53–55] This technique produces MXenes with similar surface terminations, but the presence of interlayer water molecules in the resulting materials can prolong drying time and reduce stability. Furthermore, surface terminations influence interlayer spacing; for example, hydrophobic fluorine groups reduce spacing and water retention.[55]

Another etching technique known as alkaline treatment etches the A layer using strong bases such as sodium hydroxide (NaOH) or potassium hydroxide (KOH). Though slower and less effective than HF techniques, it is less toxic and environmentally benign.[56] In this method, an HF-free approach for synthesis MXenes with fluorine-free terminations has evolved as etching MAX phases using concentrated alkali solutions. Reacting MAX phases such as Ti_3AlC_2 with concentrated NaOH at elevated temperatures (270 °C) removes aluminum atoms and produces hydrophilic hydrogen oxide surface groups.[57] Improved hydrophilicity allows this method to achieve 214% higher mass capacitance than HF-etched MXenes.[57] But handling concentrated alkaline solutions and high-temperature reactions creates safety issues that complicate scaling for industrial manufacture.[57,58] Usually displaying multilamellar "accordion-like" structures, the resulting MXenes,[57,59] need further processing steps including chemical interaction with agents such as tetrabutylammonium hydroxide (TBAOH) and dimethyls sulfoxide (DMSO) to increase interlayer spacing and mechanical delamination through sonication to isolate single-layer nanosheets.[59] These post-processing needs complicate matters more than other synthesis methods like molten-salt etching.[60]

Molten salt etching is another emerging approach, leveraging low-melting-point salts such as chlorides and carbonates to promote uniform diffusion and dissolution of reactants. This technique allows for lower reaction temperatures and high product purity.[61,62] This method might lessen the requirement for pre-treatment with ball milling. Metal chlorides, carbonates, nitrates, and fluorides are among the frequently utilized molten salts.[63] Using mild solutions like sodium chloride (NaCl) or HCl, electrochemical etching uses a three-electrode system including a MAX phase material as the working electrode. Although this approach avoids dangerous chemicals and is safer, it takes more processing time.[64,65] Salt etchants involve the use of molten salts, for example potassium fluoride (KF) or LiF at high temperatures to etch the A layer. It is effective for

nitride-based MXenes but results in smaller flake sizes and lower crystallinity.[66,67]

Although this strategy reduces environmental hazards and facilitates recycling, challenges such as carbide-derived carbon (CDC) formation, intercalator toxicity, and poor scalability still hinder industrial application.[68] Optimization of parameters like voltage, time, and electrolyte concentration is ongoing. Thermo-assisted etching may offer better control, but reproducibility remains an issue. Guan *et al.* introduced a microwave-assisted molten salt method to synthesize Ti_3AlC_2 powders. This process, using a mixture of titanium hybride (TiH_2), aluminum, titanium carbide (TiC), and NaCl/KCl, achieved up to 98.5% purity at lower temperatures with shorter reaction times, demonstrating the synergy between microwave heating and molten salts.[61]

2.2.2. Bottom-up synthesis. Unlike the top-down approach, the bottom-up method builds MXene from smaller molecular precursors. This technique enables more precise control over flake dimensions, surface chemistry, and structure.[69] The growth of sheets from specific precursors using three widely used techniques, chemical vapor deposition (CVD), template method, and plasma-enhanced pulsed layer deposition (PEPLD), is the mainstay of the bottom-up approach.[31,42]

Using gaseous precursors, CVD is a high-precision technique that creates MXenes by depositing layers on substrates such as silicon or copper.[70,71] Although it has a limited yield and is expensive, it produces high-quality, crystalline MXene films.[42] Using transition metal oxide (TMO) nanosheets as templates, the template method transforms them into MXenes *via* ammoniation or carbonization.[42] Although it takes longer to process, this method is more economical and produces higher yields than CVD.[72] Wang *et al.* established a direct synthesis methodology for the large-scale and cost-efficient manufacturing of MXenes by interaction between metal halides/metals with methane, nitrogen, or graphite. This method enables the CVD fabrication of MXenes and spherulite structures.[73]

Chuan Xu *et al.* fabricated ultrathin molybdenum carbide (Mo_2C) crystals using CVD, enabling low-temperature synthesis of superconducting 2D materials.[74] In contrast, Zhang *et al.* used PEPLD to produce uniform face-centered cubic (FCC)-Mo_2C films with tunable thickness by adjusting laser pulse frequencies and methane plasma intensity.[75] While PEPLD allows fine control over film morphology, the crystallinity and throughput are typically lower than CVD.

2.2.3. Green synthesis. In response to environmental concerns, green synthesis approaches have been developed to eliminate toxic reagents and reduce ecological impact.[76–80] These methods often utilize benign substances such as NaOH, zinc chloride ($ZnCl_2$), sodium tetrafluoroborate ($NaBF_4$), or LiF–HCl combinations instead of HF. Electrochemical and thermal etching are also explored as chemical-free options.[64,81–83] By utilizing this process, MXenes are more biocompatible and non-toxic than those made with traditional techniques that use HF or chemicals that produce HF. If these HF-containing solutions are not disposed of properly, there is a chance that groundwater could get contaminated, which could damage aquatic ecosystems and human health by contaminating sources of drinking water.[84] Although the use of green synthesis and green technology in the production of MXene has demonstrated potential for biomedical use, their clinical translation is still limited, as is the case with many other 2D material-based biotechnologies. There are several obstacles to overcome, such as a lack of knowledge about how MXene integrates with biological systems, ambiguous biological mechanisms, and worries about possible toxicity.[85]

Table 1 provides a comparative summary of the major synthesis techniques under the three main categories including top-down, bottom-up, and green synthesis.

Table 1 Comparison of MXene synthesis techniques[86]

Synthesis type	Method	Key reagents/ conditions	Advantages	Limitations
Top-down	HF etching	HF	High yield; functional surfaces (hydrogen oxide, fluorine, and oxygen)	Highly toxic; environmental and health concerns
	LiF–HCl *in situ* HF	LiF + HCl	Safer than direct HF; similar surface terminations	Interlayer water retention; longer drying times
	Alkaline treatment	NaOH or KOH at high temperature	Fluorine-free surfaces; eco-friendlier	Requires high temp; lower yield; multiple post-processing steps
	Molten salt etching	Metal chlorides/ carbonates	High purity; low-temp synthesis	Limited scalability; low flake size
	Electrochemical etching	Salt solution + 3-electrode system	Safer; HF-free	Longer processing time; scalability challenges
Bottom-up	CVD	Gaseous precursors on substrates	High-quality, crystalline MXenes	Expensive; low yield
	Template method	TMO nanosheets + ammoniation	Higher yield than CVD; cost-effective	Complex setup; limited flake control
	PEPLD	Plasma & pulsed laser deposition	Tunable film thickness	Low throughput; lower crystallinity
Green	Green etchants (*e.g.*, $NaBF_4$, $ZnCl_2$)	Eco-friendly salts	Reduced toxicity; improved biocompatibility	Limited industrial maturity; integration challenges
	Electrochemical & thermal etching	Voltage + heat + benign electrolytes	No HF; safer disposal	Low reaction rate; reproducibility issues

2.2.4. MXene functionalization pathways. Beyond synthesis routes, surface functionalization plays a vital role in tailoring MXene properties for specific applications. The limitations of MXenes have restricted their applications due to their low mechanical flexibility, easy restacking, and poor stability in the presence of molecular oxygen. Using the enriched functional groups on the surface of materials based on MXene to create new, controllable bindings that alter the surface characteristics could be one way to solve the problem.[87–89] Recently, pristine MXenes have had their surfaces modified with covalent and non-covalent modifications to create functionalized MXenes.[88] These functionalization approaches could fall into three main categories: termination engineering, functionalization *via* small molecules, and polymer functionalization.[88]

• Functionalization *via* termination engineering

Surface terminations on MXene have a major impact on the material's stability, electronic structure, and other chemical and physical characteristics. Obtaining MXene materials with distinct structural features and properties effectively requires the controllable regulation of MXene surface terminations.[90] The physical characteristics of MXenes, such as the types and concentrations of electrochemical active sites and electronic structures, can be altered by altering their surface by regulating the T groups.[91] Oxygen and fluorine surface terminations are readily accomplished using standard etching methods like HF or fluoride-containing salts which are mentioned before. By varying the etching time and etchant concentration, as well as by employing different post-treatments like hydrazine and annealing in different atmospheres, the concentrations and kinds of surface terminations can be tuned.[52,92] For example, Halim *et al.* reported that NaOH treatment enabled low-temperature vacuum annealing (550 °C) to produce predominantly oxygen-terminated Ti_3C_2 MXene by facilitating fluorine removal, altering lattice parameters and titanium oxidation states.[93] Also, density functional theory calculations revealed that surface terminations critically influence the Fermi level density of states, with reduced fluorine concentrations during annealing (300 to 775 °C) significantly enhancing conductivity.[94] Furthermore, hydrogen annealing transformed surface groups (*e.g.*, carbon–titanium–hydroxyl [C–Ti–OH] to oxygen–titanium–oxygen/carbon–titanium–oxygen [O–Ti–O and C–Ti–O]) and generated titanium–carbon (Ti–C) vacancies, which drastically increased saturation magnetization in otherwise nonmagnetic Ti_3C_2.[95]

• Functionalization *via* small molecules

The outer surface of MXenes has a range of surface terminations that can serve as molecular anchoring points through covalent/noncovalent functionalization.[96] Small molecule functionalization significantly enhances MXene properties and applications; for instance, introducing the non-ionic surfactant hexaethylene glycol monododecyl ether ($C_{12}E_6$) onto Ti_3C_2 improved molecular interactions *via* hydrogen bonding between MXene surface groups and $C_{12}E_6$'s hydrogen oxide, leading to enhanced packing symmetry.[97] Solvothermal treatment of niobium carbide (Nb_2C) with ethanol increased surface functional groups and interlayer spacing, which promoted multiple reflections and provided polarization sites, resulting in superior electromagnetic wave (EMW) absorption performance.[98] Diazonium-based surface chemistry enabled large-scale MXene delamination by weakening M-X bonds and expanding interlayer spacing through aryl-surface linkages.[44]

• Functionalization *via* polymerization

Surface groups of MXenes enable polymer integration *via ex situ* blending—offering defined structures and tunable compositions facilitated by hydrogen bonding/electrostatic interactions—or *in situ* polymerization.[99,100] Specifically, Sun *et al.* produced highly conductive nanocomposite materials composed of MXenes embedded within a polystyrene matrix (MXene@polystyrene nanocomposites) *via* electrostatic assembly, observing that electrostatic forces dominated assembly at lower MXene contents while van der Waals forces and hydrogen bonding prevailed at higher contents.[101] Ling *et al.* fabricated Ti_3C_2/polyvinyl alcohol (Ti_3C_2/PVA) composites using hydrogen bonding and Ti_3C_2/polydiallyldimethylammonium (Ti_3C_2/PDDA) composites *via* electrostatic interactions, demonstrating intercalated and orderly stacked structures respectively.[102] For *in situ* approaches, Boota *et al.* polymerized pyrrole between Ti_3C_2 layers, forming a periodic pattern with hydrogen bonds between MXene surface groups and the polymer,[103] while Lin *et al.* functionalized Ti_3C_2 with soybean phospholipid to improve physiological stability and tumor targeting.[104] Furthermore, amino-silane modification of Ti_3C_2, inspired by Shamsabadi *et al.*'s work on titanium dioxide (TiO_2), creates covalent bonds and free amine groups enabling diverse applications.[105] Research demonstrated self-initiated photo-grafting and photopolymerization (SIPGP) can be readily performed at room temperature under UV radiation and has been successfully applied to diverse substrates including graphene, carbon nanotubes, silicon-based materials, and diamond.[106–108] Furthermore, it is indicated PEGylation *via* electrostatic adsorption is an economical and effective strategy to improve MXene's water dispersibility.[109] Additionally, a covalent modification strategy was developed employing (3-aminopropyl) triethoxysilane (APTES) as a bridge to conjugate PEG onto MXene; this approach provided dual benefits: APTES bonding to MXene hydroxyl groups enables subsequent binding to amino groups, while the APTES amino group itself reacts with PEG to form PEGylated MXene for biomedical applications.[45]

2.3. Types of MXenes

Many MXene variants including those derived from titanium (Ti–MXenes),[46,110] vanadium (V–MXenes),[111,112] molybdenum (Mo–MXenes),[113,114] tantalum (Ta–MXene),[115] and niobium (Nb–MXene)[116,117] have been investigated over the past few years; each of them shows unique properties and possible uses in different fields of science.[118] The mostly studies MXene is Ti_3C_2 because of its electrical conductivity, chemical stability, and mechanical strength.[119]

Ti_3C_2 is typically created by selectively etching the A element from MAX phases like Ti_3AlC_2. This leads to delaminated layers with adjustable surface chemistry and flexible electronic characteristics.[120] Ti_3C_2 has shown great promise in the field of biomedical sciences for antibacterial applications,[121] photothermal treatment (PTT),[122,123] and biosensor development.[124,125] Its ultrathin nanosheets exhibit a natural PTCE of 48.6%, enabling effective photothermal hyperthermia for the treatment of cancer.[126]

Vanadium-based MXenes are a different subclass of MXenes where vanadium serves as the transition metal. These nanomaterials, which belong to the larger family of 2D transition metal carbides, adhere to the general structural formula $V_{n+1}X_nT_x$, where the functional properties depend much on the surface terminations (T_x). They are generated by selectively etching MAX phases, such vanadium aluminum carbide (V_2AlC), so allowing their use in several advanced uses.[118] Algae-based extraction has shown success in intercalating and delaminating V_2AlC, producing high volume vanadium carbide (V_2C) nanosheets best fit for PTT. These V_2C nanosheets show remarkable NIR absorption and great structural integrity by achieving PTCE higher than that of other MXenes. Particularly studies using PTT have shown promising results *in vitro* and *in vivo* as well as their effectiveness in eradicating cancer cells.[127,128]

Molybdenum-based MXenes, represented by the general formula $M_{n+1}AX_n$, include molybdenum titanium carbide MXene (Mo_2TiC_2), which is derived from the MAX phase molybdenum titanium carbide molybdenum titanium aluminum carbide (Mo_2TiAlC_2).[118] Recently, these molybdenum-based MXenes, Mo_2CT_x in particular, have shown great promise in PTT.[129,130] Apart from their great absorption in the near-infrared spectrum, molybdenum-based nanomaterials (Mo-NMs) have interesting properties including high light absorption, biodegradability, low cytotoxicity, biocompatibility, and a large surface area.[129,131] These features make molybdenum-based nanomaterials strong contenders for cancer theranoscopic applications.[130,132] Moreover, advanced molybdenum-based nanocomposites were synthesized to improve the functionality of Mo-NMs, facilitating synergistic combination therapies.[131,132]

Tantalum-based MXenes display unique features resulted from their adjustable electronic and mechanical features, making them highly promising for biomedical applications like drug delivery and imaging.[133,134] Furthermore, because of their high PTCE, ultrathin 2D Ti_3C_2 MXenes show great potential in tumor ablation, so supporting efficient cancer treatment.[14]

First presented in 2013 by selectively etching MAX phases, niobium-based MXene, especially Nb_2C, led to the synthesis of layered materials with various surface functional groups.[118,135] In the NIR-I and NIR-II bio-windows, respectively, these niobium-based MXenes show amazing PTCEs of 36.4% and 45.65% respectively together with proving photothermal stability and biocompatibility.[23]

In drug delivery systems, Nb_2C nanocomposites have demonstrated high loading capacity (32.57%) and efficient cancer cell inhibition. For example, they achieved a 92.37% reduction in U87 glioblastoma cells through photothermal hyperthermia, underscoring their therapeutic potential.[136]

3. Role of MXenes in ovarian cancer diagnosis and treatment

3.1. MXenes in CA125 detection

CA125 is a type of mucin-like glycoprotein with molecular weight of about 200 kDa, regarded as the most reliable or in other words the gold standard biomarker for ovarian cancer detection.[137] It was first identified in 1981 as an antigen of ovarian carcinoma epithelial cells[138] and is observable in the blood of ovarian cancer patients. CA125 is present in more than 90% of patients with advanced epithelial ovarian cancer (stages II, III, and IV) and in 50% of individuals with early-stage cancer.[139,140] Thus, the identification of CA125 is crucial for the early diagnosis of ovarian cancer.[141]

As a diagnostic biomarker, a blood CA125 level beyond 35 U mL^{-1} is generally correlated with a heightened risk of ovarian cancer, while in healthy person, this level is below 35 U mL^{-1}.[137] Various techniques have been developed for the detection of CA125, including radioimmunoassays, colorimetric assays, electrochemical analysis, surface plasmon resonance, quartz crystal microbalance, chemiluminescence, and enzyme-linked immunosorbent assays (ELISA).[137,142] Due to the disadvantages in conventional approaches relative to contemporary alternatives, like false positive results, diminished sensitivity, and inability in trace detection in ELISAs[143] or costly apparatus in chemiluminescence,[144] novel approaches like biosensors have emerged as the superior alternative to conventional detection methods in clinical and point-of-care diagnostics in recent decades.[145–147]

Biosensors offer superior selectivity and sensitivity, enhanced mobility, and reduced sample preparation compared to conventional diagnostic methods.[148] Nanomaterials enhance the sensitivity, specialization, and rapid responsiveness of biosensors for distinct tasks.[149–151] Numerous nanomaterial and biomaterial biosensors employing various sensing modalities have been developed to detect and monitor cancer biomarkers in recent years.[152]

MXenes has changed to effective options in biomarker detection because of their high surface area and superior electrical conductivity, and also adjustable characteristics.[153,154] Due to these features, MXene-based electrochemical biosensors can detect cancer biomarkers with high sensitivity and selectivity, reaching detection limits as low as femtomolar concentrations.[154,155] The studies investigating MXene-based structures in CA125 detection in ovarian cancer are discussed in the following.

3.1.1. Electrochemical immunosensor. The most extensive category of biosensing tools for protein detection is electrochemical immunosensors made up of a transducer, a signal readout system, and a biorecognition element.[156] The two main categories of electrochemical immunosensors are labeled and non-labeled depending on their structural design; antigen–antibody binding causes a change in the electrochemical impedance signal, which the non-labeled electrochemical immunosensor uses to detect the analyte. Typically, an appropriate electroactive label (enzyme, NP, *etc.*) is needed for the labeled electrochemical instrument which has been coupled to the antibody for detection.[157] Numerous 2D layered nanomaterials, specifically MXenes, have been created and employed thus far in the production of electrochemical biosensors because of their high specific surface area, adjustable electronic structure, superior mechanical and flexible qualities.[158]

An electrochemical immunosensor was designed to detect the ovarian cancer using an immunosensor composed of a

glassy carbon electrode (GCE) functionalized with MXene, graphene QD (GQD), and Au NPs in real samples.[137] Adding Au NPs improved the absorption and increased the effective surface area performance of GCE (Fig. 1A). When the GCE was modified by MXene, GQD, and AuNPs, the currents of cyclic voltammetry (CV) peaks were increased and the electron transfer resistance was reduced in comparison to GCE alone (Fig. 1B). The bare electrode had a charge transfer resistance (R_{ct}) of 5665.97 Ω, while the modified electrode depicted R_{ct} = 322.15 Ω due to its increased conductivity. This multilayer MXene provided a wide specific surface area for a lot of Au NP attachments. The concentration of MXene-GQDs nanocomposites on the surface of GCE was optimized by various volumes of MXene-GQD suspension which 4 μL was the optimal volume. Ten calibration plots of the improved system were made in the range of −0.2 to 0.6 V and at various concentrations of CA125 antigen. High sensitivity for CA125 detection was provided by increasing the concentration of CA125, which decreased square wave voltammetry (SWV) voltammograms. For the developed immunosensor, the limit of detection (LOD) of the CA125 antigen was 0.075 nU mL^{-1} and the results demonstrated a suitable linear connection between the SWV response and the quantities of CA125 (linear range 0.1–1 nU mL^{-1}) (Fig. 1C). Analytical techniques confirmed excellent performance, stability over four days, and reproducibility (relative standard deviation [RSD] = 2.04%). The biosensor exhibited minimal interference from other biomarkers (*e.g.*, prostate-specific antigen [PSA], cancer antigen 153 [CA153]). The immunosensor was highly stable with no obvious signal decay over several days, only showing 2% reduction in the electrochemical signals after 4 days at 8 °C and about 15% after storage for 120 hours at 4 °C. Importantly, detection of CA125 in both diluted healthy serum and serum samples from ovarian cancer patients, with recovery rates ranging from 98.1 to 105%, indicated that the sensor is applicable for complex biological matrices with a certain degree of biosafety for short-term diagnostic applications. However, further evaluation of long-term toxicity and immune response is needed.[137]

The strong interlayer van der Waals forces in 2D MXenes lead to significant stacking and aggregation, which drastically lowers their specific surface area and restricts their practical performance.[159,160] A viable approach is incorporating the

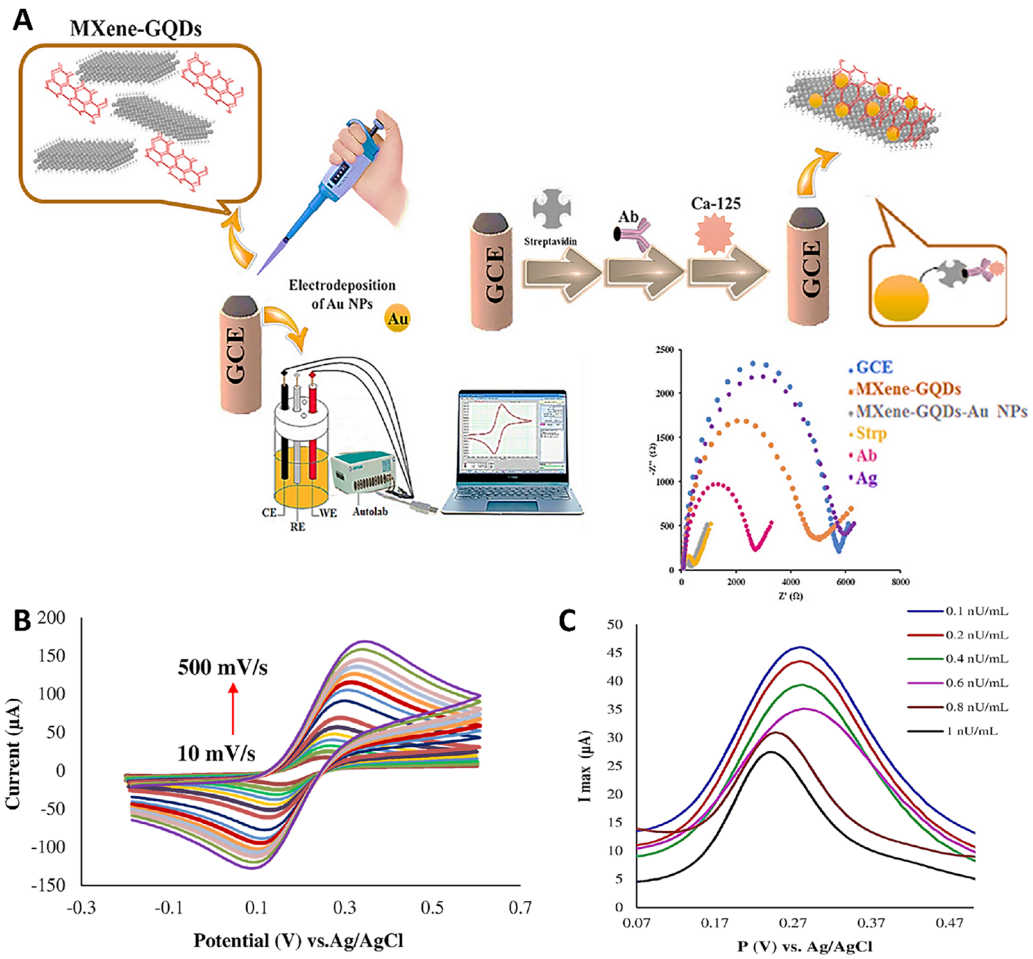

Fig. 1 (A) Schematic image of fabrication process of MXene-GQD/AuNPs immunosensor. (B) Results of sensing kinetic of fabricated sensor in the presence of different scan rates (10–500 mV s^{-1}). (C) Detection of different concentrations of CA125 in real sample. Reprinted with permission from ref. 137. Copyright 2024, The Author(s).

conductive materials between the layers of MXene that acted as spacers[161] among them is one-dimensional carbon nanotubes (CNTs) that have high electrical conductivity and excellent chemical stability.[162,163] Unfortunately, random physical mixing of MXene with CNTs does not effectively resolve the stacking issue, as both MXene and CNTs carry a negative charge. In

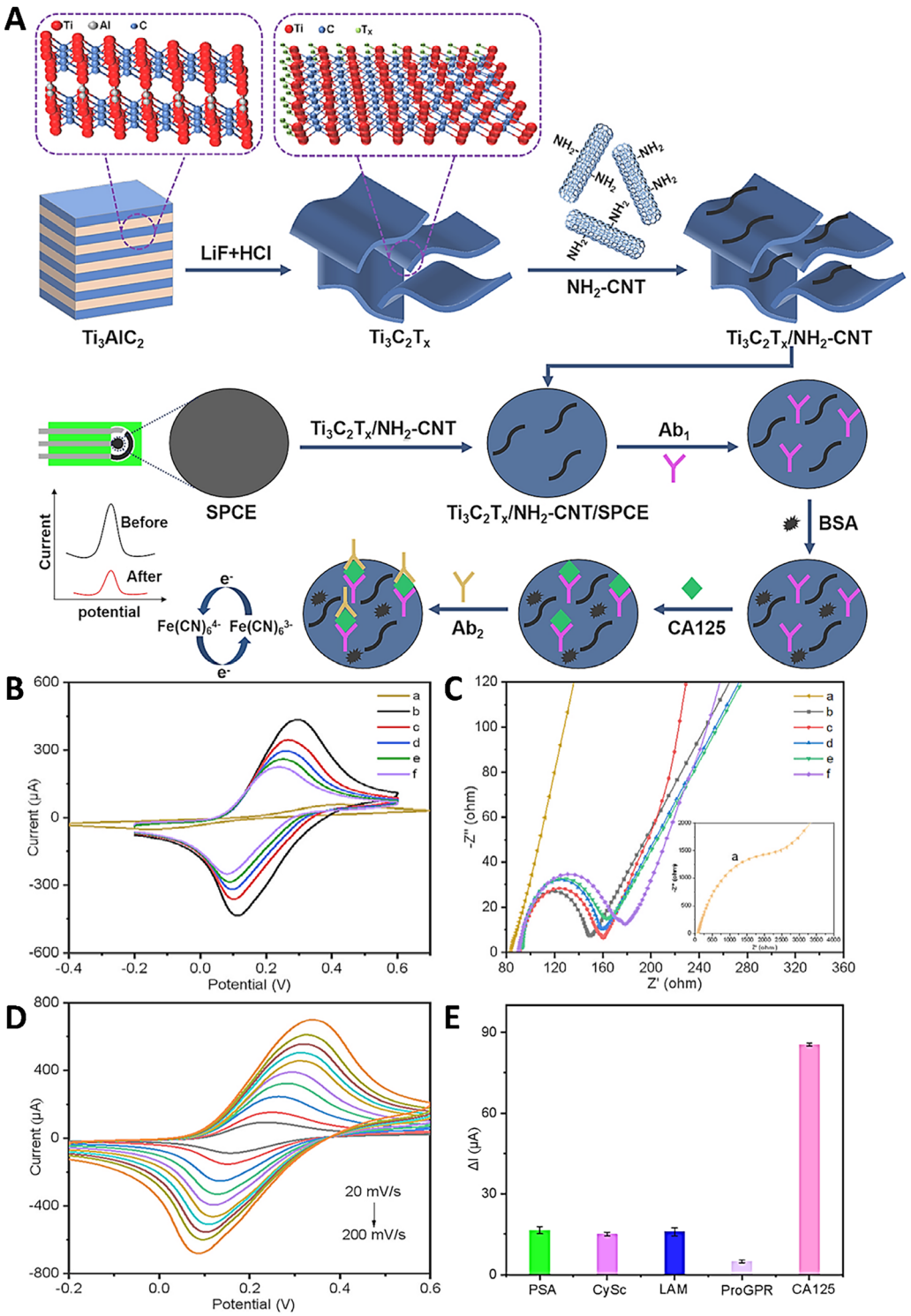

Fig. 2 (A) Schematic image of fabrication of electrochemical immunosensor used for the detection of CA125. Effect of utilizing different modifications ((a) Bare SPCE, (b) $Ti_3C_2T_x/NH_2$–CNT/SPCE, (c) Ab1/$Ti_3C_2T_x/NH_2$–CNT/SPCE, (d) BSA/Ab1/$Ti_3C_2T_x/NH_2$–CNT/SPCE, (e) CA125/BSA/Ab1/$Ti_3C_2T_x/NH_2$–CNT/SPCE, and (f) Ab2/CA125/BSA/Ab1/$Ti_3C_2T_x/NH_2$–CNT/SPCE) on sensing performance (B) and interfacial features (C) of the electrode. (D) Effect of different scan rate (20–200 mV s^{-1}) on redox peak current of $Ti_3C_2T_x/NH_2$–CNT/SPCE. (E) Assessment of the selectivity feature of the sensor in the presence of different sample. Reprinted with permission from ref. 166. Copyright 2025, Published by Elsevier.

contrast, amino-functionalized CNTs (NH_2–CNT), with positively charged, could address the stacking problem and enhance the electrochemical sensing performance of MXene.[164] Chitosan (CS), known for its excellent film-forming feature, could be used as a functionalizing agent in the structure of biosensors.[165]

A disposable ultrasensitive immunosensor was constructed based on $Ti_3C_2T_x$MXene/NH_2–CNT modified screen-printed carbon electrode (SPCE) for the detection of the CA125 in ovarian cancer (Fig. 2A).[166] The redox peak current of $Ti_3C_2T_x$/NH_2–CNT modified SPCE was significantly increased compared to bare SPCE due to its superior electronic conductivity and large active area. However, the immobilization of antibody 1 (Ab1) decreased the redox peak current due to the non-conductive biomacromolecule. After blocking non-specific active sites with bovine serum albumin (BSA), the CA125 antigen and antibody 2 (Ab2) were modified on the electrode, decreasing the redox peak current stepwise. This successful construction of a CA125 electrochemical immunosensor was confirmed by comparing the CV plots of the modified and control groups. The current signal showed significant change after adding CA125, demonstrating the immunosensor's specificity. The study demonstrated the successful construction of a CA125 electrochemical immunosensor by modifying the electrode with $Ti_3C_2T_x$/NH_2–CNT, which significantly reduced the R_{ct} of the bare SPCE (Fig. 2B and C). However, the R_{ct} was then raised when Ab1 was immobilized on the electrode surface. The R_{ct} was then raised gradually while the BSA, CA125, and Ab2 were changed one after the other on SPCE. This was explained by the fact that the electron transport between the electrode and hexacyanoferrate(III/II) $(Fe[CN]6)^{3-/4}$ was impeded by these non-conductive proteins. The use of 0.25 wt% CS solution as a dispersant enhanced the stability of the composites on the working electrode. CV tests showed that the electrode material of $Ti_3C_2T_x$/NH_2–CNT(H_2O)/SPCE behaved stably, confirming that CS could improve electrode stability (Fig. 2D). The use of CS in the experimental group greatly improved the current signal and reduced background, attributed to the formation of a homogeneous conductive network and adsorption on the electrode surface. The fabricated immunosensor displayed a wide linear detection range (1 mU mL^{-1} to 500 U mL^{-1}) and low LOD (1 mU mL^{-1}). It demonstrated good selectivity and reproducibility (RSD $\sim$ 1.04%). Clinical validation showed satisfactory alignment with chemiluminescence methods used in hospitals, with relative deviations within $\pm$8.55%. The sensor showed good selectivity for CA125, with minimal interference from other common proteins like PSA, cystatin C (CysC), and pro-gastrin releasing peptide (ProGRP). The test was conducted using 100 U mL^{-1} of CA125 and 1000 U mL^{-1} of the four interferents to bolster the results. The CA125 current signal was substantially altered in comparison to the interferents' signals, suggesting that the developed immunosensor has good selectivity for CA125 detection (Fig. 2E). Although the present study primarily focused on the analytical performance of the $Ti_3C_2T_x$/NH_2–CNT modified with CS electrochemical immunosensor, the experimental results also offered indirect insights into its biocompatibility and clinical applicability. The differential pulse voltammetry (DPV) response of the constructed immunosensor was observed on days 1, 3, 7, 14, and 21, respectively, after it was stored at 4 °C. On day 21, the sensor's activity stayed at 99.3% of its starting level indicating chemical robustness suitable for practical applications. Moreover, successful detection of CA125 in both spiked healthy serum samples and clinical serum from ovarian cancer patients—without significant deviation from the chemiluminescence method used in hospitals—suggested strong compatibility with biological fluids. The high recovery rates (85–110%) and low RSD values (1.71–7.1%) observed in serum testing further reflected its reliability in complex physiological matrices. These findings, together with the sensor's resistance to signal interference and high reproducibility, implied a promising level of biosafety and short-term operational safety. Nevertheless, further dedicated studies—including cytotoxicity assessments, immune response evaluations, and long-term *in vivo* toxicity tests—are required to comprehensively determine the biocompatibility of $Ti_3C_2T_x$/NH_2–CNT composites for clinical or implantable applications.[166]

An innovative electrochemical immunosensor was constructed using a dual MOF sandwich strategy for the detection of the CA125.[142] They fabricated immunosensor *via* combining MXene (Ti_3C_2), amino-functionalized MIL-101 MOF with iron (MIL-101(Fe)-NH_2), and zirconium-based MOF composed of zirconium oxide/hydroxide cluster coordinated by six 1,4-benzenedicarboxylate linkers ($Zr_6O_4[OH]_4[BDC]_6$ [UiO66]) loaded with methylene blue (MB). The DPV current response of composite material of MXene sheets coated with CS polymer, further integrated with MIL-101 MOF particles (MXene@CS@MIL101) was 30.63 $\pm$ 0.59 μA significantly bigger than the DPV current response of composite material of MXene sheets coated with CS polymer (MXene@CS), indicating that the MXene@CS@MIL101 composites as the base layer could amplify the electrochemical signal to improve the immunosensor performance significantly. Additionally, it showed that the MXene@CS@MIL101 composites work in concert, which could be a major factor in this immunosensor's high sensitivity. MIL-101(Fe)-NH_2 enhanced the primary antibody loading capacity, while composite of UiO66 MOF loaded or functionalized with MB (UiO66@MB) served as a signal probe for redox processes. This sensor achieved high sensitivity with LOD of 0.006 U mL^{-1} in detecting CA125. The sensitivity for the CA125 detection was calculated to be 83.26 μA mL U^{-1} cm^{-2}. The immunosensor showed potential for clinical applications, with recovery rates of 99.94–100.1% in spiked serum samples. The study focused on the detection of a single antigen (CA125) and the potential for simultaneous detection of multiple tumor markers was suggested but not explored. The results also suggested the biocompatibility and clinical feasibility of the MXene-based electrochemical immunosensor for CA125 detection. The immunosensor showed good specificity to CA125, high reproducibility (RSD $<$ 5%) and signal stability with no significant degradation or instability over a period of 72 hours storage at 4 °C, and good accuracy for detecting CA125 in patient serum samples and recovery experiments, with strong agreement compared to standard chemiluminescence assays (relative error [E_r] = 0.50–5.21%).

These results suggested that the MXene-based electrochemical immunosensor functioned well as a matrix of the nanocomposite, and can be used to detect CA125.[142]

The combination of amino-functionalized UiO66 MOF (UiO66-NH_2 MOF) and Ti_3C_2 MXenes was used in another research for CA125 detection.[167] It was a sandwich-like electrochemical immunosensor (STEM) using nanoribbon-like Ti_3C_2 MXenes ($Ti_3C_2T_x$NR) as a carrier for the primary antibody (PAb) and UiO-66-NH_2 MOFs coupled with toluidine blue (Tb) as a signal amplifier. Results of this study demonstrated a wide linear range (0.2–150.0 U mL^{-1}) and low LOD; the results showed that the Tb current peaks increased linearly between 0.2 and 150.0 U mL^{-1}, as did the increase in CA125 concentration. The linear equation was $y = 0.308 + 0.103x$ ($R^2 = 0.9983$), where x was the concentration (ng mL^{-1}) of CA125 and y was the current response (μA) of Tb. The LOD value derived from S/N = 3 was 0.05 U mL^{-1}. The current peaks' corresponding RSD was 3.22%. In the meantime, the assembled Tb-MOFs/SAb and PAb/$Ti_3C_2T_x$NR were stored at 4 °C until they were no longer useful for assessing the stability of the planned STEM test. After 35 days of storage, the trials showed that the present peak reaction shows virtually no decrease (~9.25%) with a good reproducibility (RSD = 3.22%) suggesting physicochemical robustness and low degradation in aqueous environments. Next, a 100-fold excess quantity of additional interfering chemicals, was used to examine the specificity of the STEM assay. The computed results showed that the value of $k_{i,g}$ for human serum albumin (HAS), vascular endothelial growth factor (VEGF), carcinoembryonic antigen (CEA), CA153, cancer antigen 199 (CA199), and lysozyme (Lys) were −3.25, −2.78, −3.26, −2.53, and −2.68, respectively. This indicated the superior specificity of the STEM platform for CA125. The designed STEM assay was tested in real human serum samples, with results showing adaptability in real applications. The assay measured CA125 in a local hospital sample, with recoveries ranging from 94.35–99.66%. Concurrent ELISA technology confirmed the assay's precision, indicating the compatibility of the nanomaterial interfaces in biological matrices and suitability for real sample measurement. These results indicated that this $Ti_3C_2T_x$NR and MOF-based composite platform was not likely to release toxic byproducts or cause matrix interference during short-term assays. However, as new materials for bioanalytical platforms, further investigation of their toxicity and matrix interference potential is required.[167] Additionally, self-assembled Prussian blue (PB) NPs were decorated on MXene QDs supported by electrodeposited Au NPs modified glassy carbon electrode (AuNP/PB/MXene QD/GCE) (Fig. 3A). The measurement of CA125 using DPV yielded an impressive sensitivity, with a linear range of 1 pU mL^{-1} to 0.12 nU mL^{-1} (R^2 = 0.9824) and a LOD of 0.57 pU mL^{-1}. It was in consistent with their previous findings which reported an enhanced conductivity and promoted the attachment of anti-CA125 onto the modified GCE, consequently improving sensitivity using an electrochemical immunosensor to detect the ovarian cancer using an immunosensor composed of a GCE functionalized with MXene, GQD, and AuNPs in real samples, however, this time they had added phosphate-buffered saline (PBS) because of its remarkable qualities, which include strong redox reaction activity, magnetic qualities, electrochemical traits, and photophysical effects.[137,168]

3.1.2. Surface plasmon resonance detection. MXenes have shown great potential in enhancing surface plasmon resonance (SPR) detection due to their high electrical conductivity, tunable surface chemistry, and excellent biocompatibility. When integrated into SPR sensor platforms, MXenes can improve signal sensitivity by facilitating stronger plasmonic coupling and providing abundant active sites for biomolecular binding. Their two-dimensional structure also enables efficient analyte interaction, making them suitable for label-free detection of cancer biomarkers.[169] This feature was employed in a research *via* fabricating a sandwich-like SPR imaging (SPRi) biosensor through the combination use of aptamer-functionalized MXene/iron(III) oxide (Apt-MXC/Fe_3O_4) and aptamer functionalized gold chip for

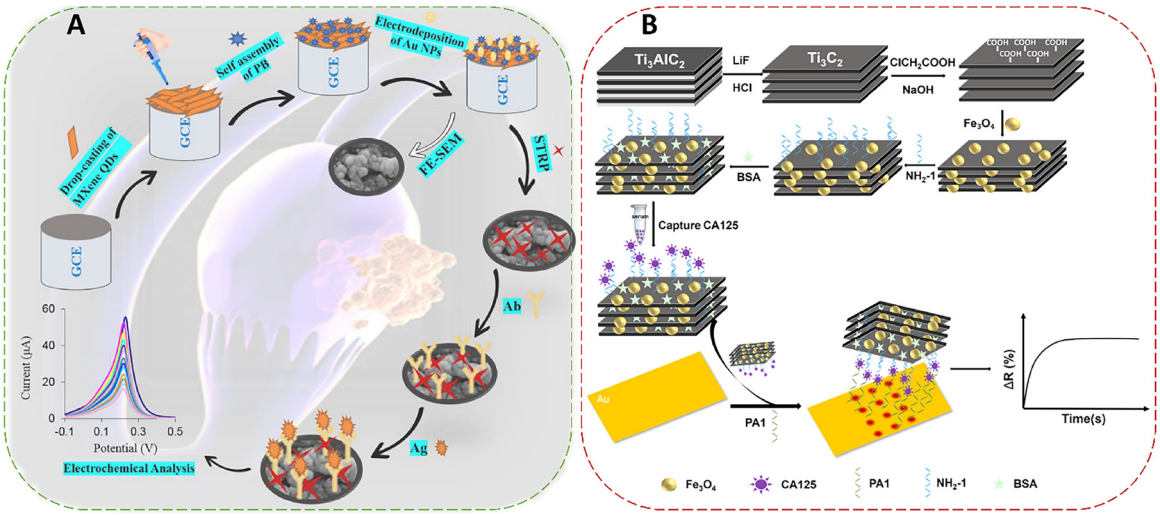

Fig. 3 Schematic images related to the fabrication and application of (A) AuNP/PB/MXene QD/GCE immunosensor (reprinted with permission from ref. 168. Copyright 2024, Elsevier B.V.) and (B) Apt-MXC/Fe_3O_4 based SPRi biosensor. Reprinted with permission from ref. 170. Copyright 2025, The Author(s).

the detection of CA125 presented in serum (Fig. 3B). A polyadenylic (polyA)-modified DNA aptamer on the surface of a gold chip particularly collected and recognized the CA125 protein. With a LOD of 0.47 nM, the biosensor showed a linear range of direct detection of CA125 based on SPRi from 20 nM to 0.5 nM. Additionally, MXC/Fe_3O_4 nanocomposites were created by synthesizing Fe_3O_4 NPs *in situ* on the carboxyl-functionalized 2D material Ti_3C_2. Ti_3C_2's vast surface area offered plenty of binding sites for the *in situ* production of Fe_3O_4, which made it easier to immobilize DNA aptamers later on. The amino-modified DNA aptamer was fixed on the surface of the MXC/Fe_3O_4 nanocomposite after interacting with carboxylate sites that were activated on the surface of Ti_3C_2. Under an external magnetic field, the CA125 protein in serum might be efficiently collected and separated thanks to the magnetic characteristics of the Fe_3O_4 NPs in the composite material. By forming a sandwich amplification structure with the DNA adaptor on the gold chip's surface, the trapped protein amplified the CA125 detection signal. With a LOD as low as 81 fM, the biosensor exhibited a linear detection range of 0.5 pM to 1000 pM. The biosensor achieved remarkable selectivity, precision, and sensitivity in detecting the ovarian cancer marker thanks to the composite nanomaterials' special separation capabilities, which allows it to detect CA125 protein as low as 1 pM in complicated liquid matrices like serum.[170]

3.2. MXenes and innovative biomarkers in ovarian cancer detection

Early detection of ovarian cancer depends on the identification of strong biomarkers devoid of invasive treatments.[171] Functionalized MXenes show the capacity to detect cancer-related proteins or nucleic acids exactly. Target biomolecules binding to the MXene surface causes observable changes in electrical signals, exactly proportional to the concentration of biomarkers. This allows for the quantification of biomarker levels, providing critical insights into cancer staging and progression.[172] Beside the MXene-based biosensors engineered to detect CA125 in ovarian cancer patients, other biomarkers are utilized to provide MXene-based biosensors for cancer detection which are discussed in the following.

3.3. Optical biosensors

According to earlier reports, endometrial, bladder, and colon cancers exhibit increased expression of the lipolysis-stimulated LSR.[173–175] Among several whey acidic protein (WAP)-domain coding genes in that area, the WAP four-disulfide core domain protein 2 (WFDC2) gene on chromosome 20q12-13 codes human epididymis protein 4 (HE4). HE4 is overexpressed in various forms of ovarian cancer and ovarian cancer cell lines. The role of HE4 in early detection of ovarian cancer has been previously studied.[176–180]

A pressure-colorimetric biosensor was developed for ovarian cancer diagnosis by detecting HE4 (Fig. 4A). Through the use of Nb_2C MXene and Ag–polysulfide hybrids (Ag–S_x) hybrids, the biosensor converted photothermal effects into visual color changes and pressure elevation, enabling highly sensitive detection through a multi-signal readout system. The modification of Nb_2C MXene with Ag–S_x improved the photothermal property of the MXene (from 27.8 °C to 66.7 °C in the absence and presence of Ag–S_x) (Fig. 4B). Moreover, it could affect the UV-visible spectra of Nb_2C MXene *via* changing the light absorption from 900 nm to about 808 nm (Fig. 4C). Superior sensitivity over current methods was provided by the LOD, which was 3.01×10^{-7} ng mL^{-1} for pressure analysis and 4.86×10^{-6} ng mL^{-1} for colorimetric analysis. The rolling amplification mechanism improved signal conversion under NIR light, allowing for precise and quick detection. Indeed, the Nb_2C MXene absorbed the NIR light and led to increase the temperature on the surface of multifunctional signal conversion paper (MSCP). This led to converting the Ag–glutathione (Ag-GSH) compounds into the Ag–S_x on the MSCP, and their attachment to the MXene. As more Ag–S_x was formed, the heating effect increases in a cycle, enhancing the system's overall performance (Fig. 4D). Moreover, the concentration of Nb_2C MXene had also affect changing the temperature so that higher concentration of MXene led to greater temperature increased and a visible color change from pale yellow to dark brown (Fig. 4E). Besides the high photothermal conversion efficiency and catalase-mimicking activity of the Nb_2C MXene/Ag–S_x hybrid, biocompatibility and long-term safety are also important considerations for advancing toward clinical or point-of-care applications. The *in situ* synthesis of Ag–S_x on Nb_2C MXene through mild NIR-induced decomposition of Ag–GSH avoided strong chemical reagents that may leave cytotoxic residues during the fabrication process and enhance the biocompatibility. In addition, the self-limiting rolling deposition mechanism provided localized signal amplification without the need for continuous external chemical inputs to minimize systemic exposure and improve *in vivo* adaptability. The stable pressure and colorimetric outputs over several cycles with low RSD (4.5% for colorimetric and 3.76% for pressure analysis) indicated that the material was stable under repetitive thermal and catalytic stress. Importantly, negligible interferences from other species were observed.[181]

A highly sensitive fluorescence quenching-based immunoassay was developed for the detection of HE4 using a modified fluorescent quencher. The system employed a carboxymethyl cellulose (CMC)–functionalized Nb_2C MXene nanocomposite (CMC@MXene) to effectively quench the fluorescence of Tb-norfloxacin coordination polymer NPs (Tb-NFX CPNPs). In the assay, CMC@MXene was functionalized with HE4 antigen (Ag) and immobilized with antibody (Ab) in a 96-well plate, enabling an indirect competitive format. The addition of Tb-NFX CPNPs facilitated the transduction of biomolecular interactions into fluorescence signals. Upon NIR exposure, localized heating from the Ag–CMC@MXene composite further suppressed the emission intensity. This dual-mode quenching effect enabled highly selective and sensitive detection of HE4, with a broad linear range (10^{-5} to 10 ng mL^{-1}), low detection limit of 3.3 fg mL^{-1}, and recovery rate between 98.4–101.5%. The assay leveraged the aggregation-induced emission (AIE) characteristics of Tb-NFX and the dual role of CMC@MXene, as both a quencher and a protein carrier. This well-engineered platform demonstrated strong performance in real sample analysis and offers a promising

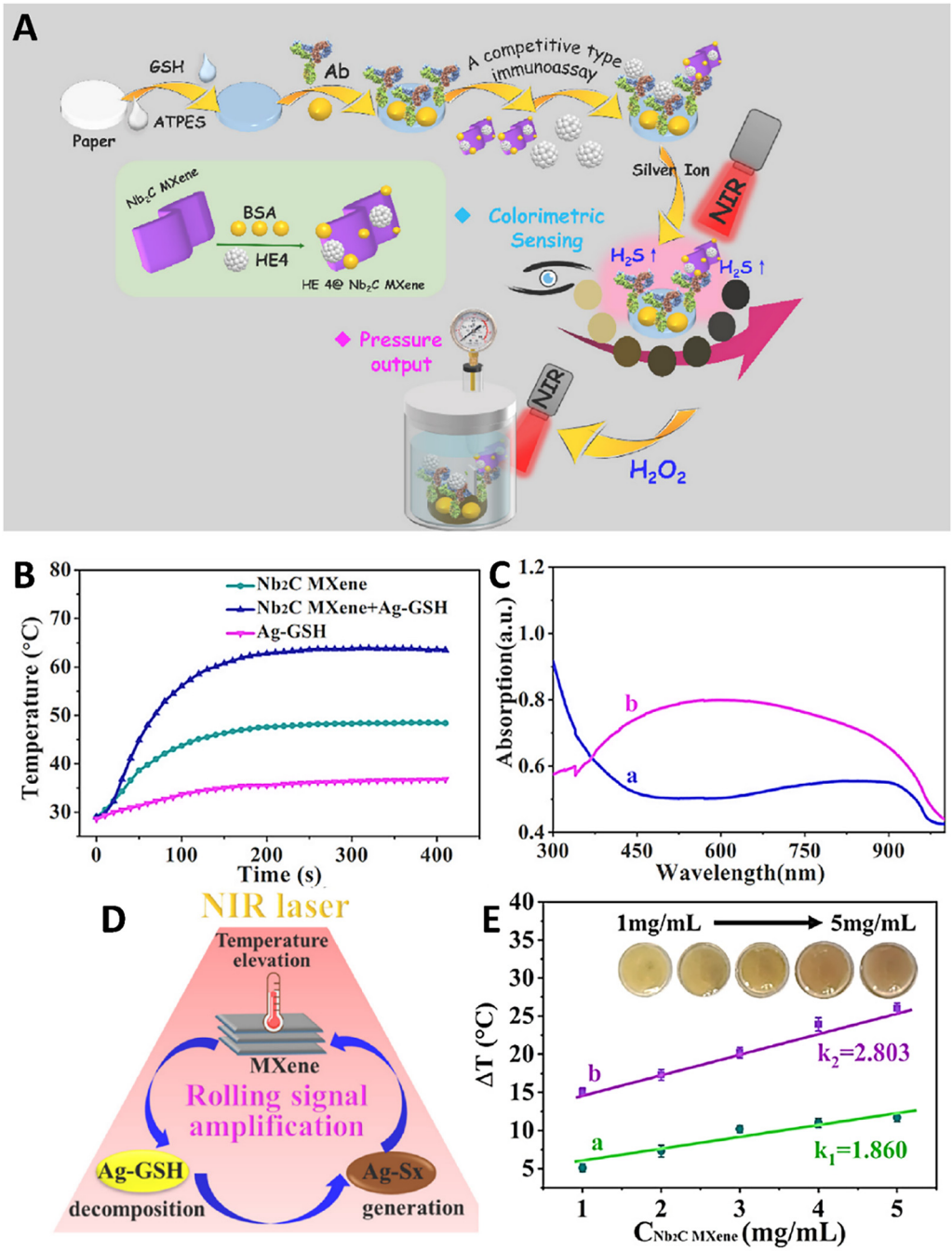

Fig. 4 (A) Schematic image related to the fabrication and biosensing application of multimodal photothermal platform, (B) photothermal profiles of a thermally sensitive Ag-GSH complex, Nb_2C MXene, and combination of Nb_2C MXene and Ag-GSH irradiated with NIR light (1.8 W cm^{-2}), (C) UV-visible spectra of Nb_2C MXene (a) and Nb_2C MXene/Ag–S_x (b), (D) schematic image of the effect of laser irradiation on enhancing photothermal effect of Nb_2C MXene/Ag–S_x, (E) effect of laser irradiation on increasing temperature of different concentrations of Nb_2C MXene (a) and MSCP (b). Reprinted with permission from ref. 181. Copyright 2023, Published by Elsevier.

approach for extending fluorescent biosensing strategies to other biomarkers.[182]

3.4. Electrochemical biosensors

The excretion of hydrogen peroxide (H_2O_2) was elevated in cancer cells, as previously observed. The release of H_2O_2 has been documented in the triggering of cellular apoptosis. Cancer cells typically do not secrete H_2O_2; but, following the introduction of a stimulant, they can leak H_2O_2 due to altered intracellular redox homeostasis.[183,184] Nagarajan *et al.* conducted a study to develop a biocompatible MXene-based biosensor for H_2O_2 detection in ovarian cancer diagnosis. They utilized a novel electrode, where flavin adenine dinucleotide (FAD) was immobilized on 2D MXene (Ti_3C_2), improving

electron transfer and catalytic properties. The biosensor exhibited LOD of about 0.7 nM and a broad linear range of 5 nM to 2 μM for H_2O_2. The biosensor operated by electrocatalytically reduction of H_2O_2 *via* the FAD/Ti_3C_2-modified electrode at −0.47 V, a significant improvement over bare electrode. The hydrophilic surface terminations on Ti_3C_2 enhanced the adsorption of FAD and stably immobilized it without any other binders, and the FAD/$Ti_3C_2T_x$-modified GCEs maintained a high electrocatalytic activity toward H_2O_2 reduction with little current loss (<2%) after 50 potential cycles and maintained 87% repeatability after three days in physiological buffers, suggesting strong structural and functional stability. In addition, the fabricated biosensor exhibited high selectivity (>98%) in the presence of common biomolecular interferents and demonstrated a capacity for H_2O_2 detection in ovarian cancer cell lines with good recovery (92–97.7% after spiking), demonstrating both diagnostic potential and biointerface stability. However, these results also confirmed that Ti_3C_2-based MXene was biocompatible and functionally robust under biological conditions, and the long-term *in vivo* fate, immunogenicity, and degradability of this material remain to be elucidated.[185]

A sensitive detection method was developed for epithelial ovarian cancer by targeting the carcinoembryonic antigen-related cell adhesion molecule 5 (CEACAM5) tumor marker using a DNA nanobiosensor. They utilized an electrochemical biosensor based on a nanocomposite of MXene multi walled CNTs polypyrrole (MXene/MWCNTs/PPY), which displayed high sensitivity (93.3%) and specificity in detecting CEACAM5 in 26 clinical samples. The biosensor had a wide linear range (5×10^{-11} to 5×10^{-7} M), low LOD (0.12 pM), and stability for up to 20 days. The biosensor functioned through the immobilization of single-stranded DNA probes on a modified electrode, facilitating hybridization with target DNA and electrochemical detection using methylene blue as an indicator. MXenes enhanced the biosensor's performance by increasing conductivity and surface area, enabling efficient electron transfer. This approach demonstrated potential as a low-cost, rapid, and non-invasive method for early epithelial ovarian cancer diagnosis. The stability and real sample analysis indirectly assessed the biocompatibility and safety profile of the fabricated MXene/MWCNTs/PPY-based electrochemical DNA biosensor but no direct cytotoxicity assays were reported. The stable electrochemical performance over 25 days and reliable detection of target DNA in complex biological matrices suggested that the nanocomposite did not undergo rapid degradation or induce interfering side effects in these settings, while the successful detection of the target with high recovery rates (87–111%) and low RSDs (<2%) in serum indicated a low level of non-specific interactions and minimal matrix toxicity, which implied acceptable biocompatibility for diagnostic applications. However, no direct *in vitro* or *in vivo* toxicity studies were conducted.[186]

3.5. Multimodal biosensors

In a recent study, a compact, multimodal sensor was developed *via* integrating optical, electrical, and visual detection components through assembling three sub-sensors capable of independently responding to NIR light. The system utilized photothermal properties of V_2C MXene QDs (MQDs) combined with polyaniline and $NiFe_2O_4$ to modulate luminescence, color, and resistance outputs within a multilayer chip. This chip comprised thermochromic paper and a thermoelectric module layered beneath a transparent indium tin oxide (ITO) electrode functionalized with a ECL probe. The V_2C MQDs contributed to strong luminescence, while $NiFe_2O_4$ enhanced electrocatalytic activity, enabling sensitive ECL signal generation. Upon NIR irradiation, the probe converted light to heat, triggering ECL enhancement, visible color change in $CoCl_2{\cdot}6H_2O$-based thermochromic paper, and precised resistance variation *via* the thermoelectric layer. This light-responsive, multi-signal platform enabled accurate detection of lipolysis-induced lipoprotein receptors across a wide linear range (10^{-6} to 10 ng mL^{-1}), showing high selectivity with LOD of about 3.3×10^{-7} ng mL^{-1}, stability (about 90.3% of its beginning values after 15 days), and reproducibility, which were comparable with other researches. In the case of real sample, the fabricated sensor showed high ECL recovery of about 99.4–101.2%. The integration of intermediate thermal modulation and signal separation provided a novel strategy for advancing multifunctional sensing technologies.[187]

An electrochemiluminescence–photothermal (ECL–photothermal) bimodal immunosensor was developed by Huang *et al.* to identify LSR as an ovarian cancer biomarker. V_2C/Ag nanocomposites, which were created by self-reducing silver ammonia on MXene nanosheets, were used in the sensor. By utilizing the complementary properties of MXene and Ag NPs, the sensor integrated ECL and photothermal detection techniques. The photothermal detection showed a linear correlation between temperature increase and LSR concentration, with a LOD of 1.53×10^{-6} ng mL^{-1}, whereas the ECL detection showed a wide linear range from 10^{-5} to 102 ng mL^{-1} with a LOD of 1.34×10^{-6} ng mL^{-1}. With recovery rates ranging from 97.8% to 107.6%, real sample analysis in human serum validated the sensor's usefulness. The PTCE was improved by the MXene/Ag nanocomposite's increased light absorption due to surface plasmon resonance (SPR) effects. In particular, V_2C/Ag had a PTCE of 27.6%, which was greater than V_2C MXene's PTCE of 26.8%. Furthermore, the biosensor's ECL response was greatly improved by the MXene/Ag nanocomposites' unexpected oxygen reduction reaction (ORR) catalytic activity. The biosensor worked by using antibodies to capture the target biomarker on a modified electrode, which allowed for dual-mode signal output when exposed to laser light. Non-specific proteins such as thyroglobulin (T_g), Interleukin-6 (IL-6), and HE4 were used to test the biosensor's selectivity. Since the ECL intensity and temperature increase (ΔT) were nearly the same as those of the blank sample, the non-specific protein was unable to impede the signal responses and the LSR assay's high specificity. Consistent photothermal behavior during multiple on/off laser cycles, reproducible ECL signals (RSD = 1.3%) and thermal readings (RSD = 2.43%), high specificity against interfering biomolecules (*e.g.*, HE4, IL-6, T_g), and high recovery rates (97.8–107.6%) in serum samples without signal suppression

indicated minimal degradation or NP leaching of the composite in aqueous conditions, as well as its compatibility with complex biological matrices. Besides showing good electrochemical and photothermal properties of the V_2C/Ag-based dual-mode immunosensor, the material design was also suitable for biocompatibility and long-term safety considerations necessary for clinical translation. The mild conditions used in the *in situ* reduction of Ag ions by V_2C MXene minimized residual oxidizing agents to facilitate cleaner synthesis with fewer toxic byproducts.[188]

Table 2 summarizes the LODs and linear range of various designed MXene-based structures in diagnosis of cancer.

3.6. Therapeutic applications of MXenes in ovarian cancer

The unique integration of electrical conductivity, optical responsiveness, magnetic behavior, and structural versatility makes MXenes a compelling platform for biomedical innovation.[196] So far, various MXene platforms have been successfully synthesized to combat malignancies.[23] Experts in biology are encouraged to contribute to this new field in order to produce more useful MXenes for a variety of uses. Among their many outstanding characteristics, they are unique and guarantee their use in biological applications in two ways: first, they have several functional groups, such as hydroxyl and oxygen, which allow them to carry a variety of drugs. Second, they are cytocompatible, which guarantees less toxicity and focused administration.[197] Because MXenes have unmatched PTCE, biocompatibility, and multifunctional engineering capabilities, they have completely changed cancer treatment. Numerous treatment techniques, such as photothermal therapy (PTT), chemodynamic therapy (CDT), photodynamic therapy (PDT), and sonodynamic therapy (SDT), are enhanced by these materials, which frequently combine several strategies to get around the drawbacks of traditional treatments.[198–210]

It was demonstrated that the engineered NP, curcumin-loaded porous MXene-derived carbon nanocarrier (PMCS) functionalized with a tumor-targeting peptide (CBP-sip65) and enhanced with the hyaluronidase enzyme PH20 (PH20/CCM@PMCS@CBP-sip65), constructed from PH20-overexpressing cancer-associated fibroblast (CAF)-cancer cell hybrid membranes and poly(dimethyl diallyl ammonium chloride) (PDDA)-modified MXene (a 2D transition metal carbide/nitride) loaded with carboplatin (CBP) and small interfering RNA targeting p65 (sip65), exhibited dual targeting of tumor cells and CAFs (Fig. 5A). Key quantitative results included 82.98% entrapment efficiency and 71.34% drug loading for CBP, and 71.79% entrapment efficiency and 1.75% loading for small interfering RNA (siRNA). NPs showed pH-dependent drug release (~70% CBP and ~50% siRNA released at pH 5.0). *In vitro*, curcumin-loaded porous carbon-based delivery system, enhanced with PH20 enzyme (PH20/CCM@PMCS) reduced cancer cell proliferation by inducing apoptosis (significant increase in Annexin V+ cells),

Table 2 The LODs and linear range of various designed MXene-based structures in diagnosis of cancer

Target biomarker	Type of MXene	LOD	Linear detection range	Ref.
CA125	GCE modified with MXene, GQDs, and AuNPs	0.075 nU mL^{-1}	0.1–1 nU mL^{-1}	137
	$Ti_3C_2T_x$–MXene/NH_2–CNT composites with CS	1 mU mL^{-1}	1 mU mL^{-1} –500 U mL^{-1}	166
	MXene (Ti_3C_2), MIL-101(Fe)-NH_2, UiO66@MB	0.006 U mL^{-1}	Not specified	142
	Ti_3C_2NR-based sandwich immunosensor with UiO-66-NH_2 MOF and TB	0.05 U mL^{-1}	0.2–150.0 U mL^{-1}	167
LSR	V_2C/Ag nanocomposites	1.34×10^{-6} ng mL^{-1} (ECL) 1.53×10^{-6} ng mL^{-1} (photothermal)	Wide detection range	188
HE4	Nb_2C MXene, Ag–S_x hybrids	3.01×10^{-7} ng mL^{-1} (pressure) 4.86×10^{-6} ng mL^{-1} (colorimetric)	Not specified	181
H_2O_2	Ti_3C_2 MXene modified with FAD	0.7 nM	5 nM–2 μM	185
CEACAM5	MXene/MWCNTs/PPY nanocomposite	0.12 pM	5×10^{-11} to 5×10^{-7} M	186
Exosomes	Iron(III) ferrocyanide [$Fe_4(Fe[CN]_6)_3$]/Ti_3C_2 MXene	229 particles μL^{-1}	5×10^2 particles μL^{-1} to 5×10^5 particles μL^{-1}	189
Exosomes	Cyanine 3-labeled aptamer specific for CD63 protein (Cy3-CD63 aptamer)/Ti_3C_2 MXenes nanocomplex	1.4×10^3 particles mL^{-1}	Not reported	190
H_2O_2	3D electrode composed of reduced graphene oxide, Ti_3C_2 MXene, and MWCNTs (3D rGO–Ti_3C_2–MWCNTs electrode)	0.3 μM	1–60 μM and 60 μM–9.77 mM	191
Cytokeratin 19 fragment 21-1 (CYFRA 21-1)	L-Cysteine functionalized magnetic NPs (L-Cyst@MNPs)/Ti_3C_2–MXene	0.023 ng mL^{-1}	0.5–30 ng mL^{-1}	192
Carcinoembryonic antigen	Functionalized Ti_3C_2 MXene nanosheets (f-Ti_3C_2–MXene)	0.000018 ng mL^{-1}	0.0001–2000 ng mL^{-1}	45
miRNA-135b	Molybdenum disulfide (MoS_2) QDs-MXene heterostructure and Au NPs coated with a biomimetic (AuNPs@biomimetic) lipid layer	10 fM	30 fM to 20 nM	193
miRNA-182	Molybdenum disulfide nanosheets decorated with Au (MoS_2@Au) NPs	6.61 am	10 am to 1 nm	194
miRNA-122	Au hollow flower-like nanostructures combined with poly(*n*-butyl acrylate (AuHFGNs/PnBA)-MXene	0.0035 aM	0.01 aM to 10 nM	195

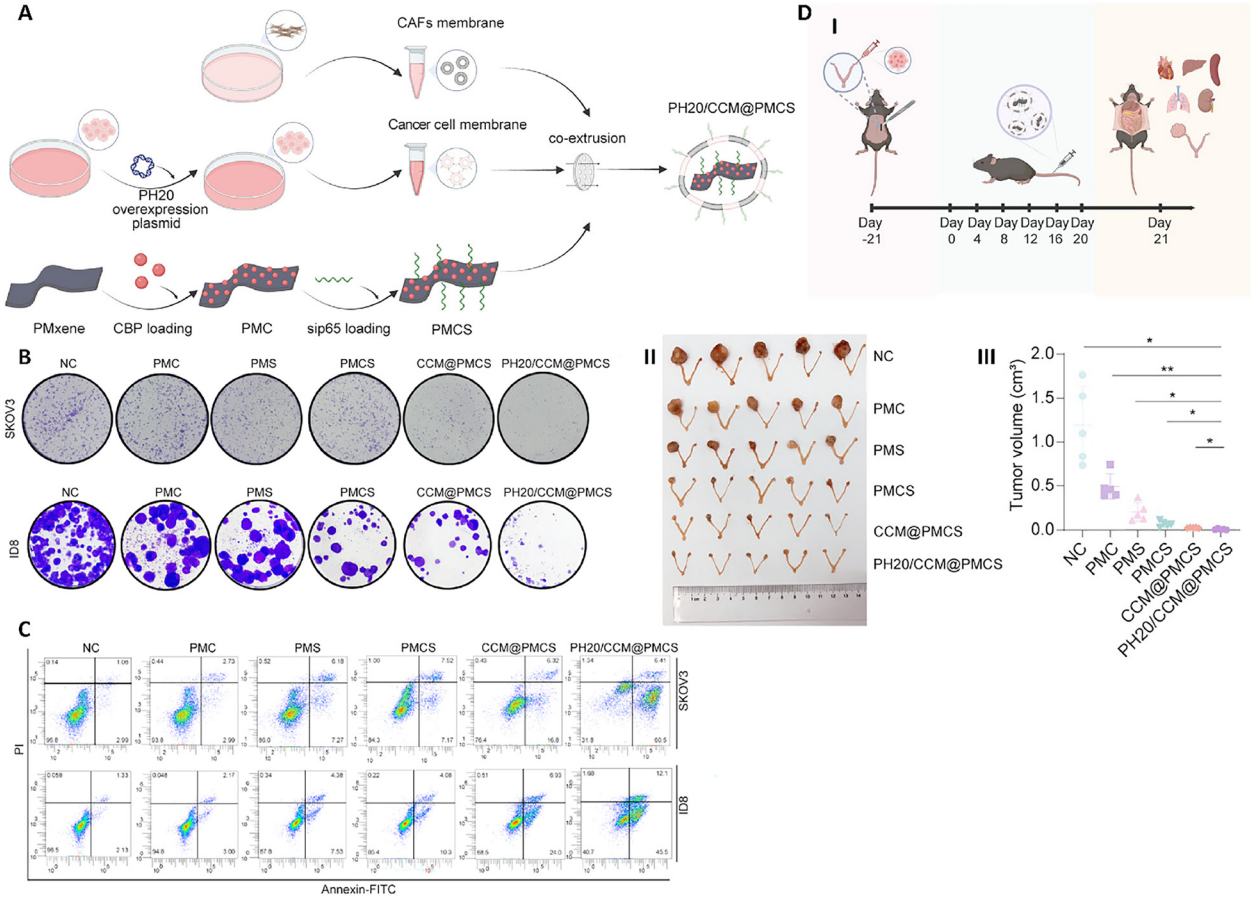

Fig. 5 (A) The production procedure of PH20/CCM@PMCS. Results of colony formation (B) and apoptotic assay (C) of different treatments (including NC, PMC, PMS, PMCS, CCM@PMCS, and PH20/CCM@PMCS on SKOV3 and ID8 cells (D) schematic illustration of *in vivo* assessment of PH20/CCM@PMCS therapeutic effect (I). Effect of different treatments on size (II) and volume (III) of tumor. Reprinted with permission from ref. 211. Copyright 2025, Published by Springer Nature.

generated reactive oxygen species (ROS), and triggered immunogenic cell death (ICD) *via* calreticulin (CRT) exposure and adenosine triphosphate (ATP)/high mobility group box 1 (HMGB1) release (2–3-fold increases in ATP and HMGB1 levels) (Fig. 5B and C). In CAFs, the NPs reduced pro-angiogenic cytokines (VEGF and angiogenin by ~50%) and increased M1 macrophage polarization (CD86+ macrophages: 14.2% → 19.3% in human, 15.4% → 55.2% in mouse models). *In vivo*, PH20/CCM@PMCS reduced tumor volume by 85.30% (*vs.* 63.37% for non-PH20-coated CCM@PMCS), decreased angiogenesis (cluster of differentiation 31 [CD31] by ~75%), and increased cytotoxic CD8+ T-cell infiltration (~50% higher activation). The NPs showed low systemic toxicity (hemolysis <5% at 10 μg mL^{-1}) and synergized with programmed death-ligand 1 (anti-PD-L1), enhancing tumor inhibition. These results highlight the platform's ability to quantitatively target multiple tumor microenvironment (TME) components, overcoming drug resistance and immune suppression in ovarian cancer (Fig. 5D). So, PH20/CCM@PMCS NPs had good biocompatibility and low toxicity both *in vitro* and *in vivo*. Cell viability assays demonstrated that PH20/CCM, PMXene, and PH20/CCM@PMXene had no cytotoxic effects on cancer cells, CAFs, and normal cell lines, suggesting the inherent safety of these coatings on cell membranes and MXene nanocarriers. Repeated intravenous injections in mice did not alter body weight or induce histopathological damage to major organs, indicating low toxicity of PH20/CCM@PMCS NPs. Hemolysis assays showed no significant red blood cell damage at working concentrations, suggesting good blood compatibility. Moreover, NP levels in plasma decreased rapidly to undetectable levels within 48 hours post-injection, while excretion analysis indicated efficient clearance by urine and feces with low NP accumulation in major organs.[211]

Yang *et al.*, conducted a study using a mouse model to investigate whether Ti_3C_2 nanosheets can translocate to the ovaries and cause ovarian damage, potentially impairing ovarian function. Results showed that intravenously injected Ti_3C_2 nanosheets were internalized by ovarian granulosa cells, reducing the number of primary, secondary, and antral follicles. This was associated with increased levels of follicle stimulating hormone (FSH), luteinizing hormone (LH), estradiol (E2), and progesterone (P4), along with decreased testosterone (T) levels. Mechanistically, Ti_3C_2 nanosheets activated autophagy *via* the phosphoinositide 3-kinase/protein kinase B/mechanistic target of rapamycin (PI3K/AKT/mTOR) pathway, with oxidative stress

playing a key role. However, autophagic flux was impaired, as indicated by increased Beclin1, autophagy-related 5 (ATG5), microtubule-associated protein 1A/1B-light chain 3 (LC3II/I) ratio, and SQSTM1 (P62) accumulation. *In vitro* experiments using KGN cells showed that inhibiting autophagy initiation with 3-methyladenine (3-MA) partially reduced estradiol and progesterone secretion, while blocking autophagic flux with Rapamycin (RAPA) exacerbated the disruption of hormone secretion. While MXene nanosheets exhibited ovarian toxicity in this context, their ability to modulate autophagy and hormonal secretion suggested potential applications in ovarian cancer treatment, particularly in leveraging autophagy-related mechanisms for targeted therapies.[210]

A study was conducted with ovarian cancer cell lines (ID8 and SKOV3) and C57BL/6 mice tumor models, aiming to develop an ultrasound-responsive bismuth molybdate (Bi_2MoO_6) MXene (BMO-MXene) heterojunction as a ferroptosis inducer for stimulating ICD against ovarian cancer (Fig. 6A). MXene was utilized in combination with Bi_2MoO_6 to form a Schottky heterojunction, synthesized through a hydrothermal method followed by mixing MXene and BMO at a 1 : 1 ratio *via* electrostatic adsorption under ultrasonication. The BMO-MXene, upon ultrasound stimulation, inhibited ovarian cancer proliferation by over 90% (Fig. 6B), induced ferroptosis through lipid peroxidation, mitochondrial membrane potential reduction, and inactivation of glutathione peroxidase (GPX4) and cystathionine transporter protein (SLC7A11), and activated ICD, enhancing dendritic cell maturation and antitumor immunity. The study found that BMO-MXene showed high ROS production and strong cytotoxicity against ovarian cancer cells *in vitro*, while *in vivo* experiments (Fig. 6C) demonstrated significant tumor volume reduction, increased ICD markers (CRT exposure, ATP secretion, HMGB1 release), and greater infiltration of immune cells such as CD8+ T cells and mature dendritic cells. It was concluded that BMO-MXene effectively induced ferroptosis and boosted antitumor immunity through ferroptosis-ICD pathway. Therefore, BMO-MXene presents a promising noninvasive, tumor-targeted ferroptosis induction strategy with immune-stimulatory effects, potentially overcoming chemotherapy resistance and enhancing ovarian cancer treatment.[209]

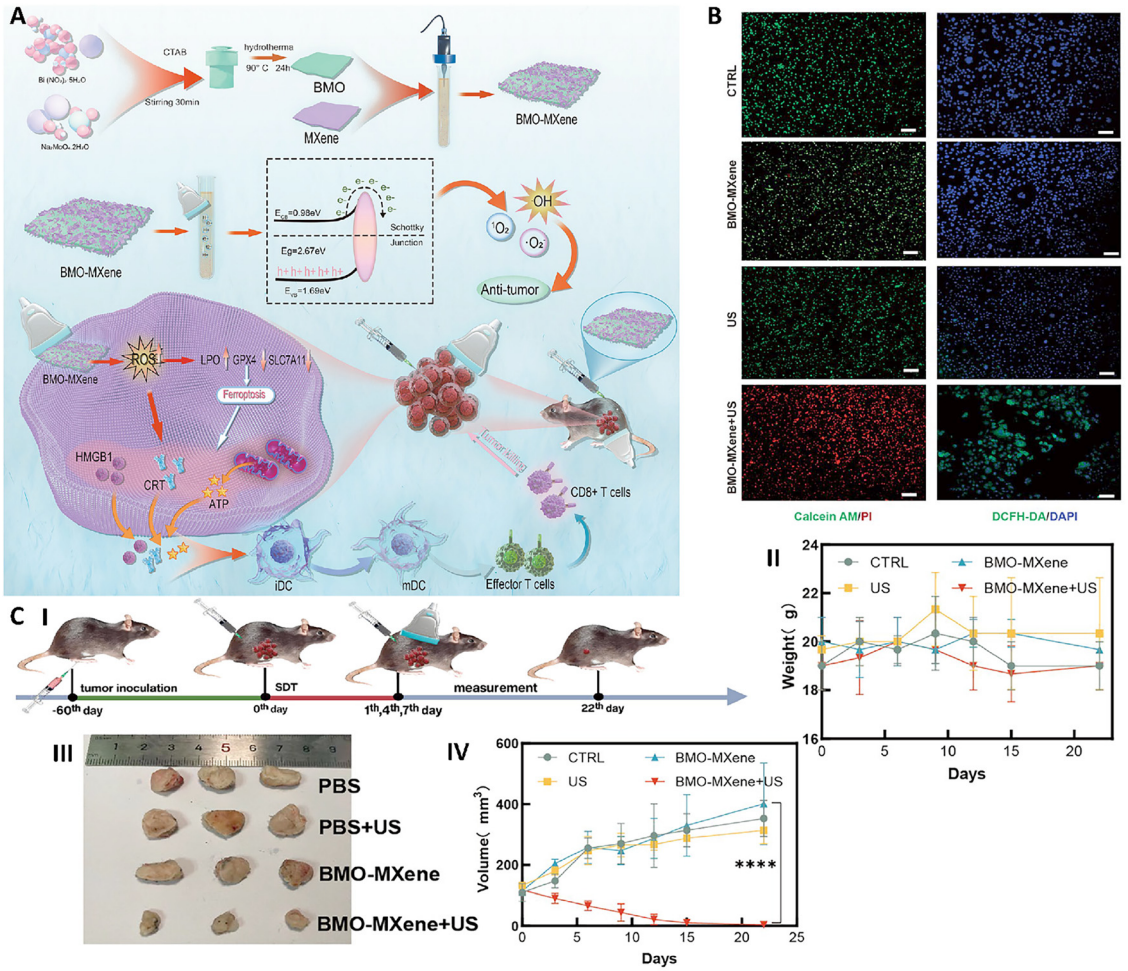

Fig. 6 (A) Schematic image related to the fabrication and anticancer application of BMO-MXene. (B) Fluorescence images of ovarian cancer cells exposed with different treatments (control, BMO-MXene, ultrasound, and the combination of BMO-MXene and ultrasonic therapy) (scar bar = 100 μm). (C) Schematic image related to *in vivo* process (I). Effect of different treatments on body weight (II), size (III), and volume (IV) of tumors exposed with different treatments. Reprinted from ref. 209 under the terms of the Creative Commons CC BY license. Copyright 2024, The Author(s).

4. Challenges and future perspectives

Nowadays, physical examination, TVUS imaging, and serum level tests for CA125 are used to diagnose ovarian cancer.[212] Findings from the prostate, lung, colorectal and ovarian (PLCO) screening trial demonstrated that testing with CA125 showed a positive predictive value of only 4%, that could be improved to 26.5% in combination with TVUS, but this combination has still not been shown to provide a noticeable improvement in survival outcomes for patients after a 15-year follow-up.[213,214] Thus, more efficient diagnostic techniques are required since CA125 screening lacks clinical sensitivity in the early stages, resulting in late-stage diagnoses and decreased survival prospects.[212]

Biomarkers are detected using conventional methods such as radioimmunoassay,[215] immune polymerase chain reaction (PCR) assay,[216] electrophoretic immunoassay,[217] mass spectrometric immunoassay,[218] and ELISA.[219] The ELISA is mostly used for the detection and determination of CA125.[220] The development of low-cost, simple, sensitive, and rapid detection techniques for point-of-care diagnosis is urgently needed due to the drawbacks of the other immunoassays, such as lengthy analysis, high cost, complex instrumentation, and the need for professional personnel, as well as the time-consuming and labor-intensive process of ELISA.[221] In recent decades, biosensors have become an important state of the art technology in laboratory medicine, notably in point-of-care diagnostics and their applications in this sector are increasing very quickly.[222]

Recent studies have demonstrated the versatility of MXene-based platforms, achieving remarkable LODs, wide linear ranges, and excellent reproducibility.[137,142,167,183] However, the severe stacking issue that 2D MXene faces as a result of the strong interlayer van der Waals force significantly lowers its specific surface area and restricts its useful performance.[159,160] The integration of MXenes with other types of nanomaterials, such as CNTs, metal NPs, MOFs, *etc.*, has significantly enhanced biosensor performance. As research progresses, MXene-based biosensors are poised to revolutionize cancer diagnostics, offering new avenues for early detection, disease monitoring, and improved patient outcomes on a global scale. Adding certain conductive elements into the MXene interlayers is a workable approach to achieve this.[161] The potential of MXene-based proposed immunosensors like what engineered by Hosseinchi Ghareaghaji *et al.*[137] in which AuNPs were added to the biosensors and showed a noticeably improved LOD and linear detection range in comparison to previous findings;[223–228] however, this study was evaluated on a small number of real samples and there is a need for more focus on developing new portable tools with the advantages of their platform that will bring benefits for point-of-care diagnostics in clinical settings. Furthermore, PB NPs, one of the many electrochemical indicators, has drawn a lot of interest because of its remarkable qualities, which include strong redox reaction activity, magnetic properties, electrochemical features, and photo-physical effects. The self-assembly method of preparing PB is simple and repeatable, which makes it appropriate for commercialization and can shorten the preparation time needed to produce immunosensors. However, PB frequently has poor conductivity, which can seriously impair the created immunosensor's functionality.[229] Some researchers have regularly used conducting AuNPs[230,231] to create PB-conducting nanocomposites in an effort to overcome these limitations and improve PB conductivity. In the field of ovarian cancer, Hosseini Ghareaghaji *et al.* reported an improved conductivity using the combination of PB and AuNP in detecting CA125.[232] Additionally, a MOF-based system was designed which successfully detected one antigen CA125. However, given its outstanding performance in this investigation, it should be able to identify numerous antigens at once. In order to enable precise and timely diagnosis of various cancers, researchers will concentrate their future efforts on developing electrochemical sensors that can concurrently detect several tumor markers in sera samples.[142] One of the limitations previously reported in the immobilization of antibodies in the immunosensor was the decreased redox peak current due to the non-conductive biomacromolecule[166] which should be considered in the future studies to overcome this hindering by antibodies for an improved conductivity in the biosensors.

Many factors influence the biocompatibility profile of MXenes, such as size, morphology, exposure duration, dosage, environmental conditions like temperature, and experimental conditions like PH. For example, in the study by Qu *et al.* pH, PBS concentration, and MB concentration all had a significant impact on an immunosensor's performance; acidic or alkaline PBS reduced the electrical signal because of the activity of antigenic and antibody proteins; neutral conditions were better for methylene blue redox reactions; the ideal pH was 7.0; PBS concentration improved peak current but decreased as concentration changed; MB concentration also had an impact, increasing proportionately with concentration; the ideal concentration was 15.0 mmol l^{-1}; and incubation time also had an impact on the sensor's performance, with peak current increasing as the incubation period was prolonged.[142] The need for systematic, standardized evaluations to check variations in safety assessments is highlighted by the fact that some studies report low toxicity under controlled parameters, such as cell line compatibility or specific incubation periods.[233,234]

One of the other challenges facing with MXene-based products is high amounts of HF or fluoride-based chemicals that are frequently used in nanosheet production techniques;[137,142,181,188] nevertheless, their toxicity restricts their effectiveness and safety precautions. This creates practical obstacles to scaling and makes large-scale production more difficult. In order to solve these problems and adhere to sustainable chemistry principles, scientists are creating green synthesis protocols that completely do away with the use of fluorine.[80,235] Optimizing these procedures is the major goal in order to guarantee scalability while preserving good production yields. The biodegradation kinetics and long-term metabolic interactions of MXenes are still poorly understood, despite their encouraging biocompatibility. Systematic investigations into their breakdown mechanisms under *in vivo* circumstances are lacking in current studies.[235] Moreover, sub-optimal drug-loading efficiency and limited spatiotemporal control limit the therapeutic potential of MXene-based nanosheets, resulting in nonspecific biodistribution and compromised

therapeutic precision; it is difficult to predict systemic biodistribution patterns because unintended dispersion can cause irreversible physiological disruptions; to mitigate off-target cytotoxicity, precise dosage control is necessary to address these biosafety concerns.[236]

In the field of treatment, because of their stability, biocompatibility, and targeting properties, MXene NPs have demonstrated promise in drug delivery and imaging applications. Stability, biocompatibility, and targeting capabilities can all be enhanced *via* surface modification. Green precursors, surface modifications using natural components, material size reduction, the use of natural ligands/linkers, and green solvents are some strategies. MXenes are useful in customized therapy because targeted delivery techniques can increase tumor tissue accumulation, decrease off-target effects, and improve drug delivery specificity.[237–239]

Converting MXenes' *in vitro* results into clinical applications requires *in vivo* studies, which assess pharmacokinetics, biodistribution, stability, and toxicity to determine safety and efficacy; balancing stability and biodegradability; assessing the environmental impact of large-scale production and disposal; and comprehending the long-term effects on human health and the environment.[238,240,241] Currently, different cell lines, different dosage schedules, and diverse experimental models all contribute to methodological inconsistencies in current research. Dual evaluation in biological contexts relevant to both health and disease is necessary for accurate safety profiling, and systematic investigations are required to establish correlations.[242]

Artificial intelligence (AI) has the potential to revolutionize cancer treatment, especially for complex malignancies like ovarian cancer. AI-driven algorithms can analyze large datasets to optimize MXene synthesis, predict biocompatibility, and customize surface modifications for targeted drug delivery. Machine learning models can help design MXene nanostructures with enhanced stability, drug loading efficiency, and controlled release profiles, improving therapeutic outcomes. For instance, Marchwiany *et al.*[243] used four ML algorithms: logistic regression, random forest, support vector machine, and extreme random tree. The results showed that only two MXenes with surface functional groups like lithium atoms and metal oxides were hazardous, indicating that the MXenes are not harmful. Additionally, by evaluating patient-specific information, such as genetic markers and tumor microenvironment profiles, AI can be used to tailor MXene-based therapies and inform the development of intelligent MXene platforms for precision medicine. AI makes it easier to understand MXene-enhanced diagnostic pictures in imaging-guided therapy, allowing for precise tumor localization and real-time therapeutic response monitoring.[244]

5. Conclusion

MXenes are a revolutionary class of 2D nanomaterials that hold great promise for the diagnosis and treatment of ovarian cancer. High surface area, conductivity, biocompatibility, and programmable surface chemistry are just a few of their remarkable physicochemical characteristics that have made them attractive options for targeted drug administration, biosensing, and imaging. By detecting well-known ovarian cancer biomarkers like CA125, HE4, LSR, and CEACAM5, advances in MXene-based biosensors have shown previously unheard-of sensitivity, opening the door to early, non-invasive diagnoses. Furthermore, there is considerable promise for improving therapy efficacy while reducing systemic toxicity by their incorporation into photothermal, photodynamic, and chemodynamic therapies.

Even with these developments, a number of obstacles still exist. Additional explorations are needed to determine the long-term toxicity and biocompatibility of MXenes, especially with regard to their stability in physiological settings and any off-target effects. For repeatability and clinical translation to be guaranteed, standardization in synthesis techniques and functionalization strategies is essential. Furthermore, further clinical trials and thorough *in vivo* research are necessary to confirm the safety and therapeutic efficacy of MXene-based theranostic techniques, even though preclinical studies have shown their efficiency. MXenes tend to undergo oxidation and degradation in biological environments, which compromises their functional integrity and therapeutic efficacy. Controlled and sustained drug release from MXene-based carriers remains difficult to achieve, limiting precise dosing and treatment duration. Moreover, comprehensive *in vivo* biosafety assessments and long-term toxicity studies are still lacking, raising concerns about potential side effects and biodegradability. Large-scale, reproducible synthesis of MXenes with consistent quality and functionalization is another significant barrier, as variability can affect clinical outcomes. Additionally, the absence of standardized regulatory guidelines and safety standards for MXene-based nanomaterials complicates their approval process for clinical use.

Future perspectives for MXenes in ovarian cancer focus on enhancing their biocompatibility and targeting capabilities through advanced surface engineering and functionalization with bioactive molecules. This could improve their selective uptake by ovarian tumor cells and reduce off-target effects. Integration with emerging technologies such as microfluidic platforms for early diagnosis and real-time monitoring could further boost their clinical utility. Moreover, combining MXene-based photothermal and photodynamic therapies with epigenetic targeting strategies, such as those addressing oncogenes like MECOM implicated in ovarian cancer chemoresistance, may provide synergistic therapeutic benefits. Integration of MXene platforms with emerging ovarian cancer biomarkers and theranostic targets, such as MUC16 and MSLN, could improve diagnostic accuracy and personalized treatment strategies. Furthermore, clinical translation will benefit from designing specialized clinical trials and regulatory frameworks tailored to the dual diagnostic and therapeutic nature of MXene-based agents. Addressing tumor heterogeneity and resistance mechanisms in ovarian cancer through MXene-enabled combination therapies, including photothermal and immunotherapies, represents a promising avenue for improving patient outcomes.

Author contributions

Neda Farzizadeh: writing – review & editing; Atefeh Zarepour: writing – review & editing; Arezoo Khosravi: visualization, graphical abstract, writing – review & editing; Siavash Iravani: supervision, conceptualization, writing – review & editing; Ali Zarrabi: supervision, writing – review & editing.

Conflicts of interest

Author(s) declare no conflict of interest.

Data availability

No data was used for the research described in the article.

References

1 X. Fu, Q. Zhang, Z. Wang, Y. Xu and Q. Dong, *Cell Death Dis.*, 2024, **15**, 21.
2 E. M. J. Ferlay, F. Lam, M. Laversanne, M. Colombet, L. Mery, M. Piñeros, A. Znaor, I. Soerjomataram and F. Bray, Cancer Today, International Agency for Research on Cancer, Lyon, France, 2022, **https://gco.iarc.who.int/media/globocan/factsheets/cancers/25-ovary-fact-sheet.pdf**.
3 Z. Momenimovahed, A. Tiznobaik, S. Taheri and H. Salehiniya, *Int. J. Women's Health*, 2019, 287–299.
4 L. M. J. Ferlay, M. Ervik, F. Lam, M. Colombet, L. Mery, M. Piñeros, A. Znaor, I. Soerjomataram and F. Bray, *Global Cancer Observatory: Cancer Tomorrow (version 1.1)*, International Agency for Research on Cancer, Lyon, France, 2022, **https://gco.iarc.fr/tomorrow/en/about#references**.
5 S. Morand, M. Devanaboyina, H. Staats, L. Stanbery and J. Nemunaitis, *Int. J. Mol. Sci.*, 2021, **22**, 6532.
6 U. M. Zamwar and A. P. Anjankar, *Cureus*, 2022, **14**, e30561.
7 Y. Xiao, M. Bi, H. Guo and M. Li, *EBioMedicine*, 2022, **79**, 104001.
8 J. R. van Nagell Jr and R. W. Miller, *Obstet. Gynecol.*, 2016, **127**, 848–858.
9 Y. Gao, S. Zeng, X. Xu, H. Li, S. Yao, K. Song, X. Li, L. Chen, J. Tang and H. Xing, *Lancet Digital Health*, 2022, **4**, e179–e187.
10 G. Moreno–Bueno, C. Gamallo, L. Pérez–Gallego, J. C. de Mora, A. Suárez and J. Palacios, *Diagn. Mol. Pathol.*, 2001, **10**, 116–122.
11 R. E. Bristow, R. S. Tomacruz, D. K. Armstrong, E. L. Trimble and F. Montz, *J. Clin. Oncol.*, 2002, **20**, 1248–1259.
12 J. B. Trimbos, I. Vergote, G. Bolis, J. B. Vermorken, C. Mangioni, C. Madronal, M. Franchi, S. Tateo, G. Zanetta and G. Scarfone, *J. Natl. Cancer Inst.*, 2003, **95**, 113–125.
13 M. Barani, M. Bilal, F. Sabir, A. Rahdar and G. Z. Kyzas, *Life Sci.*, 2021, **266**, 118914.
14 S. Shurbaji, N. P. A. Manaph, S. M. Ltaief, A. R. Al-Shammari, A. Elzatahry and H. C. Yalcin, *Front. Nanotechnol.*, 2021, **3**, 689718.
15 S. Ranjbari, M. Darroudi, B. Hatamluyi, R. Arefinia, S. H. Aghaee-Bakhtiari, M. Rezayi and M. Khazaei, *Front. Bioeng. Biotechnol.*, 2022, **10**, 984336.
16 Q. Lin, J. Li, Z. Abudousalamu, Y. Sun, M. Xue, L. Yao and M. Chen, *Int. J. Nanomed.*, 2024, **19**, 9351–9370.
17 H. Wang, J. Sun, L. Lu, X. Yang, J. Xia, F. Zhang and Z. Wang, *Anal. Chim. Acta*, 2020, **1094**, 18–25.
18 M. Darroudi, K. Ghasemi, M. Rezayi and M. Khazaei, *Mini-Rev. Med. Chem.*, 2023, **23**, 1033–1049.
19 Y. Ma, K. Jiang, H. Chen, Q. Shi, H. Liu, X. Zhong, H. Qian, X. Chen, L. Cheng and X. Wang, *Acta Biomater.*, 2022, **149**, 359–372.
20 X. Han, J. Huang, H. Lin, Z. Wang, P. Li and Y. Chen, *Adv. Healthcare Mater.*, 2018, **7**, 1701394.
21 P. Zhang, X.-J. Yang, P. Li, Y. Zhao and Q. J. Niu, *Soft Matter*, 2020, **16**, 162–169.
22 B. Zhu, J. Shi, C. Liu, J. Li and S. Cao, *Ceram. Int.*, 2021, **47**, 24252–24261.
23 H. Lin, S. Gao, C. Dai, Y. Chen and J. Shi, *J. Am. Chem. Soc.*, 2017, **139**, 16235–16247.
24 X. Yu, X. Cai, H. Cui, S.-W. Lee, X.-F. Yu and B. Liu, *Nanoscale*, 2017, **9**, 17859–17864.
25 H. Lin, Y. Chen and J. Shi, *Adv. Sci.*, 2018, **5**, 1800518.
26 S. Iravani and R. S. Varma, *ACS Biomater. Sci. Eng.*, 2021, **7**, 1900–1913.
27 S. Iravani and R. S. Varma, *Nanomaterials*, 2022, **12**, 3360.
28 G. Jamalipour Soufi, P. Iravani, A. Hekmatnia, E. Mostafavi, M. Khatami and S. Iravani, *Comments Inorg. Chem.*, 2022, **42**, 174–207.
29 F. Mohajer, G. Mohammadi Ziarani, A. Badiei, S. Iravani and R. S. Varma, *Micromachines*, 2022, **13**, 1773.
30 M. Naguib, M. Kurtoglu, V. Presser, J. Lu, J. Niu, M. Heon, L. Hultman, Y. Gogotsi and M. W. Barsoum, *MXenes*, Jenny Stanford Publishing, 2023, pp. 15–29.
31 T. Qin, Z. Wang, Y. Wang, F. Besenbacher, M. Otyepka and M. Dong, *Nano-Micro Lett.*, 2021, **13**, 183.
32 T. Dutta, P. Alam and S. K. Mishra, *J. Mater. Chem. B*, 2025, **13**, 4279–4312.
33 N. Hemanth and B. Kandasubramanian, *Chem. Eng. J.*, 2020, **392**, 123678.
34 A. Zarepour, Ç. Karasu, Y. Mir, M. H. Nematollahi, S. Iravani and A. Zarrabi, *Biomater. Sci.*, 2023, **11**, 6687–6710.
35 S. Wang, H. Ma, S. Ge, M. Rezakazemi and J. Han, *Mater. Sci. Eng., R*, 2025, **163**, 100925.
36 N. Xu, H. Li, Y. Gan, H. Chen, W. Li, F. Zhang, X. Jiang, Y. Shi, J. Liu and Q. Wen, *Adv. Sci.*, 2020, **7**, 2002209.
37 R. M. Ronchi, J. T. Arantes and S. F. Santos, *Ceram. Int.*, 2019, **45**, 18167–18188.
38 Z. Xiang, Y. Shi, X. Zhu, L. Cai and W. Lu, *Nano-Micro Lett.*, 2021, **13**, 150.
39 M. Malaki, A. Maleki and R. S. Varma, *J. Mater. Chem. A*, 2019, **7**, 10843–10857.
40 M. Sun, W. Ye, J. Zhang and K. Zheng, *Inorganics*, 2024, **12**, 112.
41 Y. Li, H. Shao, Z. Lin, J. Lu, L. Liu, B. Duployer, P. O. Persson, P. Eklund, L. Hultman and M. Li, *Nat. Mater.*, 2020, **19**, 894–899.
42 A. J. Borah, V. Natu, A. Biswas and A. Srivastava, *Oxford Open Mater. Sci.*, 2025, **5**, itae017.

43 M. Naguib, O. Mashtalir, J. Carle, V. Presser, J. Lu, L. Hultman, Y. Gogotsi and M. W. Barsoum, *ACS Nano*, 2012, **6**, 1322–1331.
44 H. Wang, J. Zhang, Y. Wu, H. Huang, G. Li, X. Zhang and Z. Wang, *Appl. Surf. Sci.*, 2016, **384**, 287–293.
45 S. Kumar, Y. Lei, N. H. Alshareef, M. Quevedo-Lopez and K. N. Salama, *Biosens. Bioelectron.*, 2018, **121**, 243–249.
46 K. Khan, A. K. Tareen, W. Ahmad, I. Hussain, M. U. Chaudhry, A. Mahmood, M. F. Khan, H. Zhang and Z. Xie, *Adv. Sci.*, 2024, **11**, 2303998.
47 S. Zhang, L. Meng, Y. Hu, Z. Yuan, J. Li and H. Liu, *Small*, 2024, **20**, 2308600.
48 P. Kuang, H. Deng, H. Cui, L. Chen, J. Fang, Z. Zuo, J. Deng, X. Wang and L. Zhao, *Oncotarget*, 2016, **8**, 4703.
49 Q. Luo, H. Cui, H. Deng, P. Kuang, H. Liu, Y. Lu, J. Fang, Z. Zuo, J. Deng and Y. Li, *Oncotarget*, 2017, **8**, 50430.
50 H. Guo, P. Kuang, Q. Luo, H. Cui, H. Deng, H. Liu, Y. Lu, J. Fang, Z. Zuo and J. Deng, *Oncotarget*, 2017, **8**, 85504.
51 Y. Ying, Y. Liu, X. Wang, Y. Mao, W. Cao, P. Hu and X. Peng, *ACS Appl. Mater. Interfaces*, 2015, **7**, 1795–1803.
52 O. Mashtalir, M. Naguib, B. Dyatkin, Y. Gogotsi and M. W. Barsoum, *Mater. Chem. Phys.*, 2013, **139**, 147–152.
53 X. Wang, C. Garnero, G. Rochard, D. Magne, S. Morisset, S. Hurand, P. Chartier, J. Rousseau, T. Cabioc'h and C. Coutanceau, *J. Mater. Chem. A*, 2017, **5**, 22012–22023.
54 Z. Lin, D. Barbara, P.-L. Taberna, K. L. Van Aken, B. Anasori, Y. Gogotsi and P. Simon, *J. Power Sources*, 2016, **326**, 575–579.
55 Y. Wei, P. Zhang, R. A. Soomro, Q. Zhu and B. Xu, *Adv. Mater.*, 2021, **33**, 2103148.
56 J. Xuan, Z. Wang, Y. Chen, D. Liang, L. Cheng, X. Yang, Z. Liu, R. Ma, T. Sasaki and F. Geng, *Angew. Chem.*, 2016, **128**, 14789–14794.
57 S. Bai, M. Yang, J. Jiang, X. He, J. Zou, Z. Xiong, G. Liao and S. Liu, *npj 2D Mater. Appl.*, 2021, **5**, 78.
58 J. Wu, Y. Yu and G. Su, *Nanomaterials*, 2022, **12**, 828.
59 K. Arole, S. E. Pas, R. M. Thakur, L. A. Amiouny, M. H. Kabir, M. Dujovic, M. Radovic, J. L. Lutkenhaus, M. J. Green and H. Liang, *ACS Appl. Mater. Interfaces*, 2024, **16**, 64156–64165.
60 M. Mim, K. Habib, S. N. Farabi, S. A. Ali, M. A. Zaed, M. Younas and S. Rahman, *ACS Omega*, 2024, **9**, 32350–32393.
61 K. Guan, W. Lei, H. Wang, X. Liu, J. Luo, Q. Jia, H. Zhang and S. Zhang, *Ceram. Int.*, 2022, **48**, 16357–16363.
62 T. Galvin, N. Hyatt, W. Rainforth, I. Reaney and D. Shepherd, *J. Eur. Ceram. Soc.*, 2018, **38**, 4585–4589.
63 H. Liu, Y. Wang, L. Yang, R. Liu and C. Zeng, *J. Mater. Sci. Technol.*, 2020, **37**, 77–84.
64 W. Sun, S. Shah, Y. Chen, Z. Tan, H. Gao, T. Habib, M. Radovic and M. Green, *J. Mater. Chem. A*, 2017, **5**, 21663–21668.
65 C. Zhou, X. Zhao, Y. Xiong, Y. Tang, X. Ma, Q. Tao, C. Sun and W. Xu, *Eur. Polym. J.*, 2022, **167**, 111063.
66 P. Urbankowski, B. Anasori, T. Makaryan, D. Er, S. Kota, P. L. Walsh, M. Zhao, V. B. Shenoy, M. W. Barsoum and Y. Gogotsi, *Nanoscale*, 2016, **8**, 11385–11391.
67 H. Yu, Y. Wang, Y. Jing, J. Ma, C. F. Du and Q. Yan, *Small*, 2019, **15**, 1901503.
68 U. U. Rahman, M. Humayun, U. Ghani, M. Usman, H. Ullah, A. Khan, N. M. El-Metwaly and A. Khan, *Molecules*, 2022, **27**, 4909.
69 A. Parihar, A. Singhal, N. Kumar, R. Khan, M. A. Khan and A. K. Srivastava, *Nano-Micro Lett.*, 2022, **14**, 100.
70 A. K. Patel, A. J. Borah and A. Srivastava, *Oxford Open Mater. Sci.*, 2023, **3**, itad020.
71 R. Dutt, R. R. Srivastava, H. Mishra and A. Srivastava, *Opt. Mater.*, 2024, **149**, 115050.
72 Y. Xie, D. Kocaefe, C. Chen and Y. Kocaefe, *J. Nanomater.*, 2016, **2016**, 2302595.
73 D. Wang, C. Zhou, A. S. Filatov, W. Cho, F. Lagunas, M. Wang, S. Vaikuntanathan, C. Liu, R. F. Klie and D. V. Talapin, *Science*, 2023, **379**, 1242–1247.
74 C. Xu, L. Wang, Z. Liu, L. Chen, J. Guo, N. Kang, X.-L. Ma, H.-M. Cheng and W. Ren, *Nat. Mater.*, 2015, **14**, 1135–1141.
75 F. Zhang, Z. Zhang, H. Wang, C. H. Chan, N. Y. Chan, X. X. Chen and J.-Y. Dai, *Phys. Rev. Mater.*, 2017, **1**, 034002.
76 I. Ijaz, E. Gilani, A. Nazir and A. Bukhari, *Green Chem. Lett. Rev.*, 2020, **13**, 223–245.
77 M. Huston, M. DeBella, M. DiBella and A. Gupta, *Nanomaterials*, 2021, **11**, 2130.
78 A. Gour and N. K. Jain, *Artif. Cells, Nanomed., Biotechnol.*, 2019, **47**, 844–851.
79 S. Jadoun, R. Arif, N. K. Jangid and R. K. Meena, *Environ. Chem. Lett.*, 2021, **19**, 355–374.
80 T. Amrillah, *Cryst. Growth Des.*, 2022, **22**, 4640–4660.
81 C. Peng, P. Wei, X. Chen, Y. Zhang, F. Zhu, Y. Cao, H. Wang, H. Yu and F. Peng, *Ceram. Int.*, 2018, **44**, 18886–18893.
82 Y. Guo, S. Jin, L. Wang, P. He, Q. Hu, L.-Z. Fan and A. Zhou, *Ceram. Int.*, 2020, **46**, 19550–19556.
83 S.-Y. Pang, Y.-T. Wong, S. Yuan, Y. Liu, M.-K. Tsang, Z. Yang, H. Huang, W.-T. Wong and J. Hao, *J. Am. Chem. Soc.*, 2019, **141**, 9610–9616.
84 S. Jolly, M. P. Paranthaman and M. Naguib, *Mater. Today Adv.*, 2021, **10**, 100139.
85 A. Rafieerad, W. Yan, A. Amiri and S. Dhingra, *Mater. Des.*, 2020, **196**, 109091.
86 S. Sezen, A. Zarepour, A. Zarrabi and S. Iravani, *Microchem. J.*, 2023, **193**, 109258.
87 B. Xu, C. Zhi and P. Shi, *J. Phys. Mater.*, 2020, **3**, 031001.
88 M. Mozafari and M. Soroush, *Mater. Adv.*, 2021, **2**, 7277–7307.
89 J. Chen, Q. Huang, H. Huang, L. Mao, M. Liu, X. Zhang and Y. Wei, *Nanoscale*, 2020, **12**, 3574–3592.
90 M. Tang, J. Li, Y. Wang, W. Han, S. Xu, M. Lu, W. Zhang and H. Li, *Symmetry*, 2022, **14**, 2232.
91 C. Wang, S. Chen and L. Song, *Adv. Funct. Mater.*, 2020, **30**, 2000869.
92 R. Thakur, A. VahidMohammadi, J. Moncada, W. R. Adams, M. Chi, B. Tatarchuk, M. Beidaghi and C. A. Carrero, *Nanoscale*, 2019, **11**, 10716–10726.
93 J. Halim, I. Persson, P. Eklund, P. O. Persson and J. Rosen, *RSC Adv.*, 2018, **8**, 36785–36790.

94 J. L. Hart, K. Hantanasirisakul, A. C. Lang, B. Anasori, D. Pinto, Y. Pivak, J. T. van Omme, S. J. May, Y. Gogotsi and M. L. Taheri, *Nat. Commun.*, 2019, **10**, 522.
95 D. Zhang, S. Wang, R. Hu, J. Gu, Y. Cui, B. Li, W. Chen, C. Liu, J. Shang and S. Yang, *Adv. Funct. Mater.*, 2020, **30**, 2002471.
96 N. Parra-Muñoz, M. Soler and A. Rosenkranz, *Adv. Colloid Interface Sci.*, 2022, **309**, 102792.
97 Y. Xia, T. S. Mathis, M.-Q. Zhao, B. Anasori, A. Dang, Z. Zhou, H. Cho, Y. Gogotsi and S. Yang, *Nature*, 2018, **557**, 409–412.
98 Z. Jin, Y. Fang, X. Wang, G. Xu, S. Wei, C. Zhou, Y. Zhang and Y. Xu, *J. Colloid Interface Sci.*, 2019, **537**, 306–315.
99 Q. Gao, X. Wang, D. W. Schubert and X. Liu, *Adv. Nanocompos.*, 2024, **1**, 52–76.
100 L. Qin, Q. Tao, X. Liu, M. Fahlman, J. Halim, P. O. Persson, J. Rosen and F. Zhang, *Nano Energy*, 2019, **60**, 734–742.
101 R. Sun, H. B. Zhang, J. Liu, X. Xie, R. Yang, Y. Li, S. Hong and Z. Z. Yu, *Adv. Funct. Mater.*, 2017, **27**, 1702807.
102 Z. Ling, C. E. Ren, M. Q. Zhao, J. Yang, J. M. Giammarco, J. Qiu, M. W. Barsoum and Y. Gogotsi, *Proc. Natl. Acad. Sci. U. S. A.*, 2014, **111**, 16676–16681.
103 M. Boota, B. Anasori, C. Voigt, M.-Q. Zhao, M. W. Barsoum and Y. Gogotsi, *Adv. Mater.*, 2016, **28**, 1517–1522.
104 H. Lin, X. Wang, L. Yu, Y. Chen and J. Shi, *Nano Lett.*, 2017, **17**, 384–391.
105 A. A. Shamsabadi, F. Seidi, E. Salehi, M. Nozari, A. Rahimpour and M. Soroush, *J. Mater. Chem. A*, 2017, **5**, 4011–4025.
106 M. Seifert, A. H. Koch, F. Deubel, T. Simmet, L. H. Hess, M. Stutzmann, R. Jordan, J. A. Garrido and I. D. Sharp, *Chem. Mater.*, 2013, **25**, 466–470.
107 P. Xiao, C. Wan, J. Gu, Z. Liu, Y. Men, Y. Huang, J. Zhang, L. Zhu and T. Chen, *Adv. Funct. Mater.*, 2015, **25**, 2428–2435.
108 N. A. Hutter, A. Reitinger, N. Zhang, M. Steenackers, O. A. Williams, J. A. Garrido and R. Jordan, *Phys. Chem. Chem. Phys.*, 2010, **12**, 4360–4366.
109 Z. Li, H. Zhang, J. Han, Y. Chen, H. Lin and T. Yang, *Adv. Mater.*, 2018, **30**, 1706981.
110 S. Shah, I. Mubeen, E. Pervaiz, H. Nasir and S. Ahsan, *Chem. Pap.*, 2023, **77**, 5601–5621.
111 Z.-L. Tan, J.-X. Wei, Y. Liu, F. U. Zaman, W. Rehman, L.-R. Hou and C.-Z. Yuan, *Rare Met.*, 2022, **41**, 775–797.
112 P. Asen, *J. Energy Storage*, 2025, **105**, 114601.
113 L. Zhao and B. Li, *Tungsten*, 2020, **2**, 176–193.
114 J. Wang, Q. Qin, F. Li, Y. Anjarsari, W. Sun, R. Azzahiidah, J. Zou, K. Xiang, H. Ma and J. Jiang, *Carbon Lett.*, 2023, **33**, 1381–1394.
115 Y. S. Worku, L. L. Sikeyi, A. S. Olaleru, T. H. Dolla, N. Palaniyandy and M. M. Mathe, *ChemistrySelect*, 2025, **10**, e202405649.
116 P. A. Rasheed, R. P. Pandey, F. Banat and S. W. Hasan, *Matter*, 2022, **5**, 546–572.
117 A. Arjun, M. Ankitha, N. Shabana, P. Vaishag, F. Shamsheera, M. Mufeeda and P. A. Rasheed, *FlatChem*, 2023, **41**, 100538.
118 D. L. Pawara, R. S. Tade, S. N. Nangare, P. O. Patil, P. K. Deshmukh, B. A. Vyas, S. B. Bari and M. P. More, *J. Ind. Eng. Chem.*, 2024, **145**, 1–19.
119 X. Cheng, L. Zu, Y. Jiang, D. Shi, X. Cai, Y. Ni, S. Lin and Y. Qin, *Chem. Commun.*, 2018, **54**, 11622–11625.
120 M. Anayee, C. E. Shuck, M. Shekhirev, A. Goad, R. Wang and Y. Gogotsi, *Chem. Mater.*, 2022, **34**, 9589–9600.
121 H. Chen, Y. Wang, X. Chen, Z. Wang, Y. Wu, Q. Dai, W. Zhao, T. Wei, Q. Yang and B. Huang, *Molecules*, 2024, **29**, 2902.
122 G. Perini, A. Rosenkranz, G. Friggeri, D. Zambrano, E. Rosa, A. Augello, V. Palmieri, M. De Spirito and M. Papi, *Biomed. Pharmacother.*, 2022, **153**, 113496.
123 C. Yu, S. Sui, X. Yu, W. Huang, Y. Wu, X. Zeng, Q. Chen, J. Wang and Q. Peng, *Colloids Surf., B*, 2022, **217**, 112663.
124 R. Kumar and L. Singh, *Adv. Mater. Technol.*, 2022, **7**, 2200151.
125 B. Ran, C. Chen, B. Liu, M. Lan, H. Chen and Y. Zhu, *Electrophoresis*, 2022, **43**, 2033–2043.
126 Z. Liu, M. Zhao, H. Lin, C. Dai, C. Ren, S. Zhang, W. Peng and Y. Chen, *J. Mater. Chem. B*, 2018, **6**, 3541–3548.
127 S. Zada, W. Dai, Z. Kai, H. Lu, X. Meng, Y. Zhang, Y. Cheng, F. Yan, P. Fu and X. Zhang, *Angew. Chem., Int. Ed.*, 2020, **59**, 6601–6606.
128 J. Wu, H. Yin, X. Song, M. Deng, B. Wang, X. Fei, J. Zhu, Z. Guo, H. Zhang and W. Chen, *Adv. Funct. Mater.*, 2024, **34**, 2313997.
129 N. Li, Y. Wang, Y. Li, C. Zhang and G. Fang, *Small*, 2024, **20**, 2305645.
130 Z. Huang, X. Cui, S. Li, J. Wei, P. Li, Y. Wang and C.-S. Lee, *Nanophotonics*, 2020, **9**, 2233–2249.
131 E. A. Hussein, M. M. Zagho, B. R. Rizeq, N. N. Younes, G. Pintus, K. A. Mahmoud, G. K. Nasrallah and A. A. Elzatahry, *Int. J. Nanomed.*, 2019, **14**, 4529–4539.
132 Z. Zhou, X. Li, T. Hu, B. Xue, H. Chen, L. Ma, R. Liang and C. Tan, *Adv. NanoBiomed Res.*, 2022, **2**, 2200065.
133 P.-S. Ganesh and S.-Y. Kim, *J. Ind. Eng. Chem.*, 2022, **109**, 52–67.
134 H. Lin, Y. Wang, S. Gao, Y. Chen and J. Shi, *Adv. Mater.*, 2018, **30**, 1703284.
135 M. Naguib, J. Halim, J. Lu, K. M. Cook, L. Hultman, Y. Gogotsi and M. W. Barsoum, *J. Am. Chem. Soc.*, 2013, **135**, 15966–15969.
136 X. Han, X. Jing, D. Yang, H. Lin, Z. Wang, H. Ran, P. Li and Y. Chen, *Theranostics*, 2018, **8**, 4491.
137 Z. H. Gharehaghaji, B. Khalilzadeh, H. Yousefi and R. Mohammad-Rezaei, *Microchim. Acta*, 2024, **191**, 418.
138 R. C. Bast Jr, T. L. Klug, E. S. John, E. Jenison, J. M. Niloff, H. Lazarus, R. S. Berkowitz, T. Leavitt, C. T. Griffiths and L. Parker, *N. Engl. J. Med.*, 1983, **309**, 883–887.
139 I. Jacobs and R. C. Bast Jr, *Hum. Reprod.*, 1989, **4**, 1–12.
140 D. Gupta and C. G. Lis, *J. Ovarian Res.*, 2009, **2**, 1–20.
141 P. S. Pakchin, M. Fathi, H. Ghanbari, R. Saber and Y. Omidi, *Biosens. Bioelectron.*, 2020, **153**, 112029.
142 L. Qu, M. Wu, L. Zhao, J. Li and H. Pan, *Microchim. Acta*, 2023, **190**, 147.

143 Q. Zhao, D. Lu, G. Zhang, D. Zhang and X. Shi, *Talanta*, 2021, **223**, 121722.
144 P. D. Mehta, B. A. Patrick, D. L. Miller, P. K. Coyle and T. Wisniewski, *J. Alzheimer's Dis.*, 2020, **78**, 1237–1244.
145 X. Huang, Y. Zhu and E. Kianfar, *J. Mater. Res. Technol.*, 2021, **12**, 1649–1672.
146 V. S. Sivasankarapillai, A. K. Somakumar, J. Joseph, S. Nikazar, A. Rahdar and G. Z. Kyzas, *Nano-Struct., Nano-Objects*, 2020, **22**, 100457.
147 H. Li, 3rd International Academic Exchange Conference on Science and Technology Innovation (IAECST), 2021, pp. 1515–1519.
148 V. Naresh and N. Lee, *Sensors*, 2021, **21**, 1109.
149 M. H. Hooshiar, M. A. Moghaddam, M. Kiarashi, A. Y. Al-Hijazi, A. F. Hussein, H. A. Alrikabi, S. Salari, S. Esmaelian, H. Mesgari and S. Yasamineh, *J. Biol. Eng.*, 2024, **18**, 28.
150 M. Li, R. Singh, Y. Wang, C. Marques, B. Zhang and S. Kumar, *Biosensors*, 2022, **12**, 843.
151 P. Malik, R. Gupta, V. Malik and R. K. Ameta, *Measurement: Sens.*, 2021, **16**, 100050.
152 M. Pourmadadi, A. Moammeri, A. Shamsabadipour, Y. F. Moghaddam, A. Rahdar and S. Pandey, *Biosensors*, 2023, **13**, 99.
153 R. S. Chouhan, M. Shah, D. Prakashan, R. PR, P. Kolhe and S. Gandhi, *Diagnostics*, 2023, **13**(4), 697.
154 A. Parihar, A. Singhal, N. Kumar, R. Khan, M. A. Khan and A. K. Srivastava, *Nanomicro Lett.*, 2022, **14**, 100.
155 J. Sengupta and C. M. Hussain, *Biosensors*, 2025, **15**, 127.
156 F. Mollarasouli, S. Kurbanoglu and S. A. Ozkan, *Biosensors*, 2019, **9**, 86.
157 M. Yang, H. Lu and S. Liu, *Appl. Sci.*, 2022, **12**, 5630.
158 E. P. Nguyen, C. d C. C. Silva and A. Merkoçi, *Nanoscale*, 2020, **12**, 19043–19067.
159 Z. Wu, T. Shang, Y. Deng, Y. Tao and Q. H. Yang, *Adv. Sci.*, 2020, **7**, 1903077.
160 J. Wu, Z. Wang, S. Zhang, Q. Yang, Z. Li, X. Zang, X. Zhao, N. Shang, N. Khaorapapong and X. Xu, *Small*, 2024, **20**, 2305730.
161 Y. Cai, X. Chen, Y. Xu, Y. Zhang, H. Liu, H. Zhang and J. Tang, *Carbon Energy*, 2024, **6**, e501.
162 J. Chen, Y. Chen, S. Li, J. Yang, J. Dong and X. Lu, *Carbon*, 2022, **199**, 110–118.
163 S. Chen, J. Xu, M. Shi, Y. Yu, Q. Xu, X. Duan, Y. Gao and L. Lu, *Appl. Surf. Sci.*, 2021, **570**, 151149.
164 X. Ma, X. Tu, F. Gao, Y. Xie, X. Huang, C. Fernandez, F. Qu, G. Liu, L. Lu and Y. Yu, *Sens. Actuators, B*, 2020, **309**, 127815.
165 Q. Wang, X. Xiao, X. Hu, L. Huang, T. Li and M. Yang, *Mater. Lett.*, 2021, **285**, 129158.
166 M. Yang, L. Wang, C. Xie, H. Lu, J. Wang, Y. Li, H. Li, J. Yang, T. Zhang and S. Liu, *Talanta*, 2025, **281**, 126893.
167 X. Mei, Z. Zeng, W. Xu, H. Yang, Y. Zheng, H. Gao, C. Wu, Y. Zheng, Q. Xu and G. Wang, *Anal. Sci.*, 2024, **40**, 1081–1087.
168 Z. H. Gharehaghaji, R. Mohammad-Rezaei and B. Khalilzadeh, *Microchem. J.*, 2024, **206**, 111633.
169 Y. Xu, Y. S. Ang, L. Wu and L. K. Ang, *Nanomaterials*, 2019, **9**, 165.
170 Z. Zou, Y. Chen, R. Sun, B. Shi, L. Jiang and F. Huang, *Microchim. Acta*, 2025, **192**, 168.
171 K. Maeda, H. Sasaki, S. Ueda, S. Miyamoto, S. Terada, H. Konishi, Y. Kogata, K. Ashihara, S. Fujiwara and Y. Tanaka, *J. Ovarian Res.*, 2020, **13**, 1–9.
172 G. Jamalipour Soufi, P. Iravani, A. Hekmatnia, E. Mostafavi, M. Khatami and S. Iravani, *Comments Inorg. Chem.*, 2022, **42**, 174–207.
173 J. M. Garcia, C. Peña, V. García, G. Domínguez, C. N. Muñoz, J. Silva, I. Millán, R. Diaz, Y. Lorenzo and R. Rodriguez, *Clin. Cancer Res.*, 2007, **13**, 6351–6358.
174 M. Herbsleb, K. Birkenkamp-Demtroder, T. Thykjaer, C. Wiuf, A.-M. K. Hein, T. F. Ørntoft and L. Dyrskjøt, *BMC Med. Genomics*, 2008, **1**, 1–17.
175 H. Shimada, S. Satohisa, T. Kohno, S. Takahashi, T. Hatakeyama, T. Konno, M. Tsujiwaki, T. Saito and T. Kojima, *Oncotarget*, 2016, **7**, 27735.
176 J. Li, S. Dowdy, T. Tipton, K. Podratz, W.-G. Lu, X. Xie and S.-W. Jiang, *Expert Rev. Mol. Diagn.*, 2009, **9**, 555–566.
177 K. Huhtinen, P. Suvitie, J. Hiissa, J. Junnila, J. Huvila, H. Kujari, M. Setälä, P. Härkki, J. Jalkanen and J. Fraser, *Br. J. Cancer*, 2009, **100**, 1315–1319.
178 J. M. Escudero, J. M. Auge, X. Filella, A. Torne, J. Pahisa and R. Molina, *Clin. Chem.*, 2011, **57**, 1534–1544.
179 R. G. Moore, A. K. Brown, M. C. Miller, S. Skates, W. J. Allard, T. Verch, M. Steinhoff, G. Messerlian, P. DiSilvestro and C. Granai, *Gynecol. Oncol.*, 2008, **108**, 402–408.
180 D. Trudel, B. Têtu, J. Grégoire, M. Plante, M.-C. Renaud, D. Bachvarov, P. Douville and I. Bairati, *Gynecol. Oncol.*, 2012, **127**, 511–515.
181 Y. Chen, Y. Huang, S. Chen, L. Gao, S. Zhang, H. Dai and B. Zeng, *Talanta*, 2023, **265**, 124876.
182 L. Du, Y. Chen, Y. Huang, S. Yan, S. Zhang and H. Dai, *Microchim. Acta*, 2023, **190**, 108.
183 N. Yang, W. Xiao, X. Song, W. Wang and X. Dong, *Nano-Micro Lett.*, 2020, **12**, 1–27.
184 S. Ramaraj, M. Sakthivel, S.-M. Chen, B.-S. Lou and K.-C. Ho, *ACS Appl. Mater. Interfaces*, 2019, **11**, 7862–7871.
185 R. D. Nagarajan, P. Murugan, K. Palaniyandi, R. Atchudan and A. K. Sundramoorthy, *Micromachines*, 2021, **12**, 862.
186 S. Rajaie, M. Nasiri, A. Pasdar, M. Rezayi and M. Khazaei, *Microchem. J.*, 2023, **193**, 109016.
187 S. Zhang, Y. Huang, L. Gao, Y. Chen and H. Dai, *Biosens. Bioelectron.*, 2025, **277**, 117224.
188 Y. Huang, S. Chen, S. Zhang, L. Gao, F. Lin and H. Dai, *J. Colloid Interface Sci.*, 2024, **661**, 793–801.
189 H. Zhang, Z. Wang, F. Wang, Y. Zhang, H. Wang and Y. Liu, *Talanta*, 2021, **224**, 121879.
190 Q. Zhang, F. Wang, H. Zhang, Y. Zhang, M. Liu and Y. Liu, *Anal. Chem.*, 2018, **90**, 12737–12744.
191 S.-Q. Yu, P. Li, H.-J. Li, L.-J. Shang, R. Guo, X.-M. Sun and Q.-Q. Ren, *Biosensors*, 2024, **14**, 261.
192 M. Choramle, D. Verma, A. Kalkal, R. Pradhan, A. K. Rai and G. Packirisamy, *Anal. Methods*, 2024, **16**, 4938–4950.

193 Y. Guo, Y. Nie, P. Wang, Z. Li and Q. Ma, *Talanta*, 2023, **259**, 124559.
194 L. Liu, C. Shangguan, J. Guo, K. Ma, S. Jiao, Y. Yao and J. Wang, *Adv. Opt. Mater.*, 2020, **8**, 2001214.
195 S. Ranjbari, M. Rezayi, R. Arefinia, S. H. Aghaee-Bakhtiari, B. Hatamluyi and A. Pasdar, *Talanta*, 2023, **255**, 124247.
196 Y. Gogotsi and B. Anasori, *MXenes*, Jenny Stanford Publishing, 2023, pp. 3–11.
197 Y. Chen, L. Wang and J. Shi, *Nano Today*, 2016, **11**, 292–308.
198 W. Feng, R. Wang, Y. Zhou, L. Ding, X. Gao, B. Zhou, P. Hu and Y. Chen, *Adv. Funct. Mater.*, 2019, **29**, 1901942.
199 Y. Dong, L. Guo, L. Song, T. Liu, G. Zheng, M. Zheng and B. Li, *Int. J. Nanomed.*, 2025, 1983–1998.
200 T. Liao, Z. Chen, Y. Kuang, Z. Ren, W. Yu, W. Rao, L. Li, Y. Liu, Z. Xu and B. Jiang, *Acta Biomater.*, 2023, **159**, 312–323.
201 D. An, X. Wu, Y. Gong, W. Li, G. Dai, X. Lu, L. Yu, W. X. Ren, M. Qiu and J. Shu, *Nanophotonics*, 2022, **11**, 5177–5188.
202 P. Xiong, X. Wei, L. Zhou, W. Zhou, M. Li, Y. Ge, J. Zou, S. Peng, L. Jiang and L. Tian, *Adv. Funct. Mater.*, 2024, **34**, 2405124.
203 A. Gazzi, L. Fusco, A. Khan, D. Bedognetti, B. Zavan, F. Vitale, A. Yilmazer and L. G. Delogu, *Front. Bioeng. Biotechnol.*, 2019, **7**, 295.
204 Q. Zhang, W. Huang, C. Yang, F. Wang, C. Song, Y. Gao, Y. Qiu, M. Yan, B. Yang and C. Guo, *Biomater. Sci.*, 2019, **7**, 2729–2739.
205 X. Wang, X. Wang, Q. Yue, H. Xu, X. Zhong, L. Sun, G. Li, Y. Gong, N. Yang and Z. Wang, *Nano Today*, 2021, **39**, 101170.
206 X. Jiang, H. Wang, Y. Shen, N. Hu and W. Shi, *Sens. Actuators, B*, 2022, **350**, 130891.
207 G. Liu, J. Zhu, H. Guo, A. Sun, P. Chen, L. Xi, W. Huang, X. Song and X. Dong, *Angew. Chem., Int. Ed.*, 2019, **58**, 18641–18646.
208 B. E. Scheibe, J. K. Wychowaniec, M. Scheibe, B. Peplińska, M. Jarek, G. Nowaczyk and Ł. Przysiecka, *ACS Biomater. Sci. Eng.*, 2019, **5**, 6557–6569.
209 S. Cheng, T. Zhou, Y. Luo, J. Zhang, K. Dong, Q. Zhang, W. Shu, T. Zhang, Q. Zhang and R. Shi, *J. Nanobiotechnol.*, 2024, **22**, 408.
210 L. Yang, Z. He, L. Hu, H. Tang, Y. Geng, Q. Tan, Y. Zhang, Y. Wen, W. Wu and H. Gu, *J. Nanobiotechnol.*, 2024, **22**, 242.
211 Y. Yao, J. Zhang, K. Huang, Y. Peng, S. Cheng, S. Liu, T. Zhou, J. Chen, H. Li and Y. Zhao, *J. Nanobiotechnol.*, 2025, **23**, 83.
212 J. M. Liberto, S.-Y. Chen, I.-M. Shih, T.-H. Wang, T.-L. Wang and T. R. Pisanic, *Cancers*, 2022, **14**, 2885.
213 S. S. Buys, E. Partridge, M. H. Greene, P. C. Prorok, D. Reding, T. L. Riley, P. Hartge, R. M. Fagerstrom, L. R. Ragard and D. Chia, *Am. J. Obstet. Gynecol.*, 2005, **193**, 1630–1639.
214 P. F. Pinsky, K. Yu, B. S. Kramer, A. Black, S. S. Buys, E. Partridge, J. Gohagan, C. D. Berg and P. C. Prorok, *Gynecol. Oncol.*, 2016, **143**, 270–275.
215 S. J. Goldsmith, *Semin. Nucl. Med.*, 1975, **5**(2), 125–152.
216 K. Saito, D. Kobayashi, M. Sasaki, H. Araake, T. Kida, A. Yagihashi, T. Yajima, H. Kameshima and N. Watanabe, *Clin. Chem.*, 1999, **45**, 665–669.
217 A. C. Moser and D. S. Hage, *Electrophoresis*, 2008, **29**, 3279–3295.
218 S. Hu, S. Zhang, Z. Hu, Z. Xing and X. Zhang, *Anal. Chem.*, 2007, **79**, 923–929.
219 R. Aebersold and M. Mann, *Nature*, 2003, **422**, 198–207.
220 A. M. Yates, S. J. Elvin and D. E. Williamson, *J. Immunoassay*, 1999, **20**, 31–44.
221 N. Scholler, M. Crawford, A. Sato, C. W. Drescher, K. C. O'Briant, N. Kiviat, G. L. Anderson and N. Urban, *Clin. Cancer Res.*, 2006, **12**, 2117–2124.
222 N. Razmi and M. Hasanzadeh, *TrAC, Trends Anal. Chem.*, 2018, **108**, 1–12.
223 M. Li, M. Zhang, S. Ge, M. Yan, J. Yu, J. Huang and S. Liu, *Sens. Actuators, B*, 2013, **181**, 50–56.
224 W. Liu, C. Ma, H. Yang, Y. Zhang, M. Yan, S. Ge, J. Yu and X. Song, *Microchim. Acta*, 2014, **181**, 1415–1422.
225 L. Wu, Y. Sha, W. Li, S. Wang, Z. Guo, J. Zhou, X. Su and X. Jiang, *Sens. Actuators, B*, 2016, **226**, 62–68.
226 W. Mu, C. Wu, F. Wu, H. Gao, X. Ren, J. Feng, M. Miao, H. Zhang, D. Chang and H. Pan, *J. Pharm. Biomed. Anal.*, 2024, **243**, 116080.
227 Z. Chen, B. Li, J. Liu, H. Li, C. Li, X. Xuan and M. Li, *Microchim. Acta*, 2022, **189**, 257.
228 A. Sangili, T. Kalyani, S.-M. Chen, A. Nanda and S. K. Jana, *ACS Appl. Bio Mater.*, 2020, **3**, 7620–7630.
229 Z. Wang, H. Yang, B. Gao, Y. Tong, X. Zhang and L. Su, *Analyst*, 2014, **139**, 1127–1133.
230 G. Wang, G. Zhang, H. Huang and L. Wang, *Anal. Methods*, 2011, **3**, 2082–2087.
231 T. Yang, Y. Gao, Z. Liu, J. Xu, L. Lu and Y. Yu, *Sens. Actuators, B*, 2017, **239**, 76–84.
232 Z. Gharehaghaji, R. Mohammad-Rezaei and B. Khalilzadeh, *Microchem. J.*, 2024, **206**, 111633.
233 V. Bhardwaj, A. Kaushik, Z. M. Khatib, M. Nair and A. J. McGoron, *Front. Pharmacol.*, 2019, **10**, 1369.
234 A. Szuplewska, D. Kulpińska, M. Jakubczak, A. Dybko, M. Chudy, A. Olszyna, Z. Brzózka and A. M. Jastrzębska, *Adv. Drug Delivery Rev.*, 2022, **182**, 114099.
235 S. Nandi, D. Karati and S. Mukherjee, *Inorg. Chem. Commun.*, 2024, **170**, 113214.
236 N. Gao, J. Zhao, X. Zhu, J. Xu, G. Ling and P. Zhang, *Acta Biomater.*, 2022, **154**, 1–22.
237 S. Iravani and R. S. Varma, *Nanomaterials*, 2022, **12**, 3360.
238 B. F. Far, N. Rabiee and S. Iravani, *RSC Adv.*, 2023, **13**, 34562–34575.
239 N. Rabiee and S. Iravani, *Mater. Chem. Horiz.*, 2023, **2**, 171–184.
240 J. Huang, Z. Li, Y. Mao and Z. Li, *Nano Select.*, 2021, **2**, 1480–1508.
241 M. Liao, Q. Cui, Y. Hu, J. Xing, D. Wu, S. Zheng, Y. Zhao, Y. Yu, J. Sun and R. Chai, *Neural Regener. Res.*, 2024, **19**, 258–263.

242 A. Maleki, M. Ghomi, N. Nikfarjam, M. Akbari, E. Sharifi, M. A. Shahbazi, M. Kermanian, M. Seyedhamzeh, E. Nazarzadeh Zare and M. Mehrali, *Adv. Funct. Mater.*, 2022, **32**, 2203430.
243 M. E. Marchwiany, M. Birowska, M. Popielski, J. A. Majewski and A. M. Jastrzębska, *Materials*, 2020, **13**, 3083.
244 S. Iravani, A. Khosravi, E. Nazarzadeh Zare, R. S. Varma, A. Zarrabi and P. Makvandi, *RSC Adv.*, 2024, **14**, 36835–36851.